NASA
Technical
Paper
2956

January 1990

Measured and Predicted Aerodynamic Coefficients and Shock Shapes for Aeroassist Flight Experiment (AFE) Configuration

William L. Wells

NASA

NASA
Technical
Paper
2956

1990

Measured and Predicted Aerodynamic Coefficients and Shock Shapes for Aeroassist Flight Experiment (AFE) Configuration

William L. Wells
Langley Research Center
Hampton, Virginia

National Aeronautics and
Space Administration
Office of Management
Scientific and Technical
Information Division

Summary

The Aeroassist Flight Experiment (AFE) utilizes a 14-ft-diameter raked and blunted elliptic cone as a vehicle to carry instrumentation for approximately 12 experiments on a Shuttle-launched flight. The flight is to obtain aerodynamic and aerothermodynamic data for blunt bodies with velocities near 32 000 ft/sec at altitudes above 245 000 ft. A preflight ground-based test program was initiated to provide calibration data for computational fluid dynamics (CFD) codes that will be used in flight predictions. The data reported here are results from a part of that test program.

Static longitudinal aerodynamic coefficients, lift-to-drag ratio, and shock shapes were obtained with two model sizes of the AFE configuration with angles of attack from −10° to 10°. The effects of Mach number, Reynolds number, and normal-shock density ratio were examined by testing in two air wind tunnels at Mach 6 and Mach 10 and in one tetrafluoromethane (CF_4) wind tunnel at Mach 6. The experimental data were compared with predictions provided by an inviscid flow computer code, HALIS.

Changes in Mach number from 6 to 10 in air or in Reynolds number by a factor of 13 have little effect on the aerodynamic coefficients, shock shapes, or lift-to-drag ratio. Changes in density ratio across the normal shock from approximately 5 (air) to 12 (CF_4) have a strong effect on aerodynamic coefficients and shock detachment distance, but not on lift-to-drag ratio. The tests in air indicate that the configuration is longitudinally stable and self-trimming at an angle of attack of 3.5°. The CF_4 results indicate more stability at angles of attack less than 5° and a trim angle of −1°. The lift-to-drag ratio in air or CF_4 is 0.29 at an angle of attack of 0° and is linear with angle of attack over the range from −10° to 10°. A variation in sideslip angle from 0° to 4° has little effect on the longitudinal aerodynamic coefficients or lift-to-drag ratio. The predictions are, for the most part, in very good agreement with the measurements. Tests in CF_4 provide a better simulation of predicted flight results than do tests in air.

Introduction

Future space transportation systems will include space transfer vehicles (STV's) to ferry cargo to and from high-Earth orbit (for example, geosynchronous orbit) and low-Earth orbit where the Space Shuttle and Space Station Freedom will operate. (This class of vehicle was formerly referred to as orbital transfer vehicles, or OTV's.) Studies have shown that upon return to low-Earth orbit, the STV can carry a heavier payload when decelerated by drag during a pass through the Earth's upper atmosphere than when decelerated by retro-rockets, which require more fuel (ref. 1). The STV's designed to use the Earth's atmosphere for deceleration are generally referred to as aeroassisted space transfer vehicles, or ASTV's (formerly AOTV's). Much more information about very high-altitude, high-velocity flight is needed, however, before an actual ASTV can be optimally designed. Preparations are underway to conduct a flight experiment in which a 14-ft-diameter, simulated ASTV configuration with approximately 12 onboard experiments will be launched from the Space Shuttle and accelerated back into the atmosphere with a rocket. This Aeroassist Flight Experiment (AFE) will make a sweep through the atmosphere down to an altitude of about 245 000 ft with a velocity of nearly 32 000 ft/sec to gain aerodynamic and aerothermal information and then return to low-Earth orbit where it will be retrieved by the Space Shuttle.

The flight experiment has been proposed because the high-velocity, low-density flow environment cannot be duplicated or simulated in present test facilities nor accurately predicted by existing computational techniques. The AFE will provide an experimental data base for validation and refinement of current computational fluid dynamics (CFD) codes to be used in future ASTV designs. The flight data will also be useful for validation of procedures used to extrapolate wind-tunnel data to flight conditions. However, the AFE itself requires a data base for prediction of its flight characteristics; and present test facilities, in conjunction with the best available CFD codes, must provide this information. A preflight test program in ground-based hypersonic facilities (ref. 2) was initiated to develop an aerodynamic and aerothermodynamic data base to provide calibration data for the most recent CFD computer codes. Predictions from one of these codes are compared with the experimental data in this paper. The experimental results presented herein are a part of the ground-based test program. Other results are presented in references 3, 4, 5, and 6. The details of the rationale for the flight experiment are outlined in reference 7, and the set of experiments to be performed is described in reference 8.

This paper addresses the effects of normal-shock density ratio on shock shapes (including detachment distances) and aerodynamic characteristics of the AFE configuration at incidence in Mach 6 flow by using tetrafluoromethane (CF_4) and air as test gases. During the continuum-flow portion of the flight, the AFE vehicle is expected to experience thermochemical equilibrium values of normal-shock density ratio in the neighborhood of 17, whereas air or nitrogen hypersonic wind tunnels produce ratios of about

5 to 7. In flight, this large density ratio results from dissociation of the air as it passes into the high-temperature shock layer. This "real gas" effect has a significant impact on shock detachment distance, distributions of heating and pressure, and aerodynamic characteristics (ref. 9). The Langley Hypersonic CF_4 Tunnel provides a simulation of this phenomenon by producing a density ratio of about 12 across the shock. The Langley 20-Inch Mach 6 Tunnel provides a density ratio of 5.2 in air at comparable Mach number and Reynolds number; thus data for code calibration are provided that include the effects of density ratio. Tests were also conducted in Mach 10 air to verify that the data are independent of significant differences in Mach numbers and Reynolds numbers for the very blunt AFE configuration in hypersonic continuum flow.

Predictions included herein were provided by Mr. James K. Weilmuenster of the Space Systems Division, Langley Research Center.

Symbols

C_A	axial force coefficient, $\frac{\text{Axial force}}{q_\infty S}$
C_m	pitching moment coefficient, $\frac{\text{Pitching moment}}{q_\infty S d}$
C_{m_α}	$\Delta C_m/\Delta\alpha$ taken between $\alpha = \pm 2^\circ$, per deg
C_N	normal force coefficient, $\frac{\text{Normal force}}{q_\infty S}$
d	model base height in symmetry plane (fig. 5), in.
L/D	aerodynamic lift-to-drag ratio
M	Mach number
p	pressure, lbf/in^2
q_∞	free-stream dynamic pressure, lbf/in^2
Re	Reynolds number
S	model base area, in^2
T	temperature, °R
U	velocity, ft/sec
$\overline{X}$	moment transfer distance (fig. 3), in. (1.673 in. when $d = 3.67$ in., and 1.599 in. when $d = 2.50$ in.)
x_o, y_o	geometric stagnation point of model (fig. 5)
x/d	abscissa for shock shape plots (fig. 5)
y/d	ordinate for shock shape plots (fig.5)
$\overline{Z}$	moment transfer distance (fig. 3), in. (0.129 in. when $d = 3.67$ in., and 0.099 in. when $d = 2.50$ in.)
α	angle of attack, deg
β	sideslip angle, deg
γ	ratio of specific heats
ρ	density, lbm/ft^3

Subscripts:

B	balance
o	model geometric stagnation point
RP	rake-plane center
t	stagnation conditions
∞	free-stream conditions
2	conditions immediately behind normal shock

AFE Configuration

The AFE flight vehicle will consist of a 14-ft-diameter drag brake, an instrument carrier at the base, a solid rocket propulsion motor, and small control motors. A sketch of the vehicle is shown in figure 1. The drag brake (fig. 2), or forebody configuration, is derived from a blunted elliptic cone that is raked off at 73° to the centerline to produce a circular raked plane. A skirt having an arc radius equal to one-tenth of the rake-plane diameter and an arc length corresponding to 60° has been attached to the rake plane in an attempt to reduce aerodynamic heating around the base periphery. The blunt nose is an ellipsoid with an ellipticity of 2.0. The ellipsoid nose and the skirt are tangent to the elliptic cone surface at their respective intersections. The half angle of the original elliptic cone is 60° in the vehicle symmetry plane. Notice in figure 2 that the angle of attack referred to in this paper is with respect to the axis of the original elliptic cone. A detailed description of the forebody analytical shape is presented in reference 10.

Apparatus and Tests

Facilities

Langley 31-Inch Mach 10 Tunnel. The Langley 31-Inch Mach 10 Tunnel expands dry air through a three-dimensional contoured nozzle to a 31- by 31-in. square test section to achieve a nominal Mach number of 10. The air is heated to approximately 1850°R by an electrical resistance heater, and the maximum reservoir pressure is approximately 1500 lbf/in^2. The tunnel, formerly referred to as the Langley Continuous-Flow Hypersonic Tunnel, is presently operated in the blowdown mode with nominal run times of up to 60 sec. Because of the side-mounted turret that allows model changes during tunnel operation in the continuous-flow mode, only one test-section window is available and the facility is not presently equipped with a schlieren system. Force-and-moment data can be obtained through a range of angle of attack during one run by utilizing the pitch-pause capability of the model support system. This tunnel is described in more detail in reference 11.

Langley 20-Inch Mach 6 Tunnel. The Langley 20-Inch Mach 6 Tunnel is a blowdown wind tunnel that uses dry air as the test gas. The air is heated to a maximum temperature of approximately 1100°R by an electrical resistance heater; the maximum reservoir pressure is 525 $\mathrm{lbf/in^2}$. A fixed geometry, two-dimensional contoured nozzle with parallel sidewalls expands the flow to Mach 6 at the 20- by 20-in. square test section. Two 16.5-in.-diameter clear tempered glass windows are located on opposite sides of the test section. A vertical reference line is located at one window for verification of angle of attack in schlieren photographs. The model injection mechanism allows angle-of-attack adjustments during a test. Test durations are usually 60 to 120 sec, although longer times can be easily attained by connection to auxiliary vacuum storage. A description of this facility and calibration results are presented in reference 12.

Langley Hypersonic CF_4 Tunnel. The Langley Hypersonic CF_4 Tunnel is a blowdown wind tunnel that uses tetrafluoromethane (CF_4) as the test gas. The ratio of specific heats of CF_4 is approximately 20 percent lower than air. The CF_4 is heated to a maximum temperature of 1530°R by two molten-lead-bath heat exchangers connected in parallel. The maximum pressure in the tunnel reservoir is 2600 $\mathrm{lbf/in^2}$. Flow is expanded through an axisymmetric, contoured nozzle designed to generate a Mach number of 6 at the 20-in.-diameter exit. This facility has an open jet test section with two 24- by 30-in. clear tempered glass windows on opposite sides. A vertical reference line is located at one window for verification of angle of attack in schlieren photographs. Run duration can be as long as 30 sec, but 10 sec is sufficient for most tests because the model injection system is not presently capable of changing angle of attack during a run. A detailed description of the CF_4 tunnel and calibration results are presented in reference 13. The calibration data indicate a disturbance in pitot pressure at the test-stream centerline. A 4-in.-diameter hemisphere pressure-distribution model tested 3 in. off centerline produced excellent agreement with theory, however. Consequently, it is standard procedure to test in this off-centerline location.

Models

Two aerodynamic models were fabricated and tested. The models were identical except for size; the base heights d (fig. 2) at the symmetry plane were 3.67 in. (2.2 percent scale) and 2.50 in. (1.5 percent scale). A photograph of one of the models is shown in figure 3 along with a sketch that provides information pertinent to the aerodynamic tests. Notice that the moment reference center is at the rake-plane center—a position that is convenient to locate in computer codes. The flight vehicle center of gravity may be somewhat aft of this position. Each model is made in three parts: a stainless steel forebody (aerobrake), an aluminum afterbody (instrument carrier and propulsion motor), and a stainless steel balance holder. The forebody was machined to the design size and shape within a tolerance of ±0.003 in. The balance-holder axis is parallel to the original cone axis. Although stainless steel subjects the balance to a greater tare weight than aluminum, steel was chosen as the forebody material because of its lower thermal conductivity and resistance to abrasion. Heat penetration through the blunt, shallow forebody can result in thermal gradients across the balance sensing elements, thereby compromising the calibration. The balances were water cooled and provision was made for an air gap between the balance forward end and the holder cavity surface to further reduce heat transfer. The models were fabricated with a cylindrical instrument carrier and a simulated propulsion motor. Because of recent redesign, the model afterbody differs from the current flight configuration. The instrument carrier is now a hexagonal shape to better accommodate instrumentation attachment, and the propulsion motor will be jettisoned after firing to avoid base-flow contamination.

Two shrouds (fig. 4) were built to shield the balance from base-flow closure. The first shroud is used when the afterbody is attached and the second when the afterbody is removed. The shrouds attach to the sting, and clearance is provided to avoid interference with the balance and model movement when forces or moments are applied.

Instrumentation

Aerodynamic data. Aerodynamic force-and-moment data were measured with water-cooled, strain-gage balances. Two thermocouples were installed in the water jacket surrounding the measuring elements to monitor internal thermal gradients.

Existing Langley balances were used to expedite testing. The load range for each component of the two balances (one for each model size) is presented in table I.

Shock shape data. To obtain schlieren photographs for shock shapes, z-type, single-pass mirror systems were used in both the Mach 6 air and Mach 6 CF_4 test facilities. Images were recorded on black and white film. All film was developed and enlarged to 8- by 10-in. prints.

Test Conditions and Test Matrix

The tests were conducted at nominal free-stream Mach numbers of 6 and 10 in air, and at Mach 6 in CF_4. Nominal test conditions are presented in table II. Angles of attack were varied from 10° to −10° with sideslip angle β at 0°. A number of tests were conducted at both Mach 6 and 10 in air with $\beta = 2°$ and 4°. A limited number of tests were run in CF_4 with $\beta = 3.5°$. All the shock shape data were taken at $\beta = 0°$. The afterbody was removed for some tests in CF_4. Both model sizes were tested in CF_4 and in air at Mach 10. Only the 3.67-in. model was tested in air at Mach 6.

Test Procedures

In the Langley Hypersonic CF_4 Tunnel, the model was mounted at the desired angle of attack and sideslip prior to the run. After the test-stream flow was established, the model was injected to a location 3 in. off the test-stream centerline (see "Facilities" section) where data were gathered for approximately 5 sec before the model was retracted. In either of the two air tunnels, the model was mounted at angles of attack and sideslip of 0° prior to the run. After test-stream flow was established, the model was injected to the stream centerline and then pitched to the next angle of attack (or angle of sideslip) by the pitch-pause mechanism. Data were taken while the model was stationary at each angle of attack and/or sideslip.

Data Reduction and Uncertainty

Shock Shapes

Shock shapes in the model symmetry plane were obtained from 8- by 10-in. black and white schlieren photographs. Each photograph was mounted on a plotter so that the AFE base was vertical as required by the digitizing program. To account for any variations in model size on the photographs, the model base height was measured from each photograph and entered into the digitizing program for use as a reference length. The geometric stagnation point was used to define the origin of the coordinate system (fig. 5). An optical sighting device was used to locate and record approximately 70 points along each shock, corresponding to a step size of approximately 0.06 in. on the photograph. The silhouette of the model symmetry plane was also digitized from the schlieren photograph and recorded in the same manner as the shock and in the correct relation to the shock. The digitized data from each photograph were stored in an individual computer file and later plotted by a graphics plotter. An indication of the accuracy of the process can be seen in figure 6, where at the smallest standoff distance (near the stagnation point) repeatability is within approximately 5 percent and is better at larger standoff distances.

Aerodynamics

Each of the three test facilities has a dedicated stand-alone data system. Output signals from the balances were sampled and digitized by an analog-to-digital converter and stored and processed by a computer. The rates at which the analog signals were sampled were 50 per second in the CF_4 and Mach 10 air tunnels, and 20 per second in the Mach 6 air tunnel. A single value of data reported herein represents an average of values measured for 2 sec in the CF_4 and Mach 6 air tunnels, and for 0.5 sec in the Mach 10 air tunnel. Corrections were made for model tare weights at each angle of attack and for interactions between different elements of the balances. Corrections were not made for base pressures. Output signals were related to forces and moments by a laboratory calibration that is accurate to within ±0.5 percent of the rated load for each component. The moments about the model rake-plane center reported herein have greater uncertainty than those measured at the balance moment center. The pitching moment at the balance has only the ±0.5 percent of rated-load uncertainty, whereas the moment at the rake-plane center also includes uncertainties associated with the forces included in the transfer equation. The transfer equation is

$$(\text{Pitching moment})_{RP} = (\text{Pitching moment})_{B} - (\overline{X})(\text{Normal force}) - (\overline{Z})(\text{Axial force})$$

where the subscripts RP and B denote the rake-plane center and the balance moment center, respectively. The transfer distances $\overline{X}$ and $\overline{Z}$ are defined in figure 3. In coefficient (C) form, the uncertainties (Δ) related to balance calibration are

$$\Delta C_i = \pm \frac{(0.005)\ (\text{Force rating})_i}{S q_\infty}$$

for force i,

$$\Delta C_{m,B} = \pm \frac{(0.005)\ (\text{Moment rating})}{S d q_\infty}$$

for pitching moment at balance, and

$$\Delta C_{m_{RP}} = \pm \left[(\Delta C_{m,B})^2 + \left(\Delta C_N \frac{\overline{X}}{d} \right)^2 + \left(\Delta C_A \frac{\overline{Z}}{d} \right)^2 \right]^{0.5}$$

for pitching moment at the rake-plane center.

All the terms include the free-stream dynamic pressure in the denominator so that the uncertainties are less at test conditions where q_∞ is large, that is, at higher Reynolds number than at lower Reynolds number. The smaller balance could not be used without overloading some of the components at higher Reynolds number operation, however. Balance related uncertainties in the data presented herein are tabulated in table III.

Prediction

Aerodynamic coefficients and shock shapes were computed for a limited number of cases for comparison with the measured data. The predicted values were obtained from solutions of the Euler equations by the inviscid flow-field computer code HALIS (ref. 14). The HALIS (High Alpha Inviscid Solution) code is a time-asymptotic solution of the Euler equations, where the solution space is the volume between the body surface and the bow shock wave that is treated as a time-dependent boundary. The code will handle arbitrary perfect gases (constant ratio of specific heats) or real gases in thermodynamic equilibrium. Test-stream flow conditions were used as inputs to HALIS, and free-stream pressure was used for base pressure. For the CF_4 computations, the program was modified to include the thermodynamic properties of CF_4 (ref. 15). The wind-tunnel and numerical model geometries were the same except for the region downstream of the aft corner. The numerical model was modified to prevent the onset of computational instabilities due to expansion of flow around the aft rim of the skirt. The modification was a cylindrical extension rearward from the skirt (ref. 14 and fig. 7).

Results and Discussions

Shock Shape

Typical schlieren photographs for tests in CF_4 ($\rho_2/\rho_\infty = 11.7$) and in air ($\rho_2/\rho_\infty = 5.2$) are shown in figure 8. The shock shapes for both CF_4 and air at Mach 6 are presented for $\alpha = 0°$, $\pm 5°$, and $\pm 10°$ in figure 9. As observed in figure 9, a factor of 2 increase in density ratio significantly decreases the shock detachment distance. For example, at $\alpha = 0°$, the shock detachment distance at the stagnation point in CF_4 is less than half the distance in air. In CF_4, an inflection in the shock is observed near the ellipsoid-cone juncture, which indicates a flow overexpansion process. This inflection is more pronounced at lower angles of attack (fig. 9(e)). In reference 6, measured pressure distributions over the AFE forebody at the same conditions also revealed the overexpansion; hence, the density ratio can also be expected to significantly influence the aerodynamic characteristics of the configuration. The effect of angle of attack on shock shapes in Mach 6 air is summarized in figure 10 and in Mach 6 CF_4 in figure 11. The detachment distances are greater (over most of the body) at $\alpha = 10°$ and decrease as α decreases to $-10°$. This is expected because the body presents a more blunt cross section to the oncoming flow as α increases and at $\alpha = 10°$ appears similar to a flat-faced cylinder where the flow is subsonic over the cylinder face. No effect of Reynolds number on shock characteristics was observed for the range available in these tests, shown for air in figure 12 and for CF_4 in figure 13.

Predicted shock detachment distances obtained with the HALIS code and shown in figure 14 for air and figure 15 for CF_4 are observed to be in very good agreement with measurement over the face of the forebody. The density ratio in flight is expected to be even greater than that obtained in the CF_4 tests. With the assumption of equilibrium chemistry and continuum flow (near perigee), HALIS was also used to predict the shock detachment distance in Mach 31 flight. This result is compared to the air and CF_4 data in figure 16, where the predicted flight detachment distance is observed to be much less than the CF_4 data. Rarefied and nonequilibrium flow effects not addressed by HALIS, but expected in flight, will tend to increase the detachment distance, however (see, for example, ref. 16). The flight shock detachment distance is important because it will influence radiant heating by determining the volume of radiators and their proximity to the surface. Furthermore, convective heating would also be expected to vary with detachment distance because of differences in flow chemistry (ref. 7).

Aerodynamics

The aerodynamic data from Mach 10 air tests are tabulated for four test conditions in tables IV through VII. The Mach 6 air results are presented in tables VIII and IX, and the Mach 6 CF_4 results in tables X and XI. The test Reynolds number and model used to obtain the data are indicated in each table title.

The aerodynamic coefficients C_A, C_N, and C_m and the lift-to-drag ratio L/D for a range of Reynolds number in Mach 10 air are presented as a function of angle of attack in figure 17. The balance uncertainties from table III are also shown. Within the range of measurement uncertainty, the coefficients and L/D show no significant effect of Reynolds number. The data obtained at $\mathrm{Re}_{2,d} = 17660$ have the least uncertainty and therefore are considered the best representation of the Mach 10 air results. The coefficients and L/D were computed for Mach 10 air at 5 angles of attack (0°, ±5°, and ±10°) with HALIS. A curve has been faired through the computed data to make them more distinguishable. These inviscid predictions of C_m and L/D are shown in figure 17 to agree with measurements, but C_A and C_N are underpredicted by about 5 percent for angles of attack greater than approximately −5°.

The Mach 6 air results are compared with Mach 10 air results in figure 18. All data in figure 18 were obtained with the 3.67-in. model. As expected, the comparison reveals no effect of Mach number within this range (ref. 17). Although the Mach 6 data taken at the lowest Reynolds number test condition indicate a large uncertainty band, the results are in good agreement with the other data. Apparently that uncertainty estimate is too conservative.

The effect of density ratio across the normal shock on the aerodynamic coefficients and L/D is shown in figure 19. Although the effects of M_∞ and $\mathrm{Re}_{2,d}$ have been shown previously to be insignificant, these parameters were made approximately equal for the two sets of data in figure 19. The effects of density ratio on aerodynamic coefficients are shown to be significant for angles of attack greater than approximately −5°. The coefficients C_A and C_N are affected by ρ_2/ρ_∞ proportionately, however, since L/D is not affected. Predictions from the HALIS code are included for both sets of data. The predicted data are in very good agreement with the experimental data except for the air results where the code underpredicts C_A and C_N measurements by approximately 5 percent.

The wind-tunnel results in CF_4 are believed to be a better simulation of flight data since the shock detachment distance is closer to the distance predicted for flight than it is in air (fig. 16). Early systems analysis (ref. 18) and control requirements (ref. 19) for the configuration assumed trim at $\alpha = 0°$ with $L/D = 0.30$. The present results reveal that the trim angle varies from −1° to 4° as the density ratio varies from 5 to 12, but as mentioned previously L/D is nearly independent of density ratio. The present study indicates that $L/D = 0.29$ at $\alpha = 0°$ and that there is a linear relationship with angle of attack. A good estimate of L/D at any α within $-10° \leq \alpha \leq 10°$ can be obtained from $L/D = 0.290 - 0.015\alpha$, where α is in degrees. Since the trim angle depends on ρ_2/ρ_∞, the value of L/D at trim will, of course, also depend on ρ_2/ρ_∞. The negative slope of the pitching moment coefficient (C_{m_α}) indicates that the configuration is longitudinally stable about the rake-plane center. The CF_4 data indicate a greater stability (more negative slope) than the air data for α less than 5°. The values of C_{m_α} in air and CF_4 are −0.0018 and −0.0029 per degree, respectively. In reference 14, the HALIS code was used to compute C_m as a function of α for the flight near perigee, assuming continuum flow in chemical equilibrium. The predicted C_m for flight (fig. 19(c)) is only slightly larger in magnitude than the CF_4 wind-tunnel data, and the slopes are nearly equal except for $\alpha > 5°$. In reference 14, the change in slope for CF_4 at $\alpha > 5°$ (see fig. 19(c)) is attributed to the change in extent of the subsonic region over the forebody face with increasing α. The predicted flight trim angle is only slightly greater than 0°, which is in much better agreement with the CF_4 wind-tunnel data than with the air wind-tunnel data.

To evaluate the effect of afterbody, tests were conducted with the afterbody both attached and removed in CF_4 with the same model, balance, and test conditions. A comparison of the results in figure 20 indicates that the longitudinal coefficients and L/D are identical with the afterbody on or off. The afterbody is shielded from the flow at hypersonic speeds and therefore does not affect the vehicle aerodynamics. Consequently, the data presented should represent the current vehicle with modified afterbody.

A number of tests were conducted with sideslip angles other than 0°. These results are tabulated in tables XII and XIII for Mach 10 air, in tables XIV and XV for Mach 6 air, and in table XVI for CF_4. Tests in air were with $\beta = 2°$ and 4° (negative angles at Mach 6) and in CF_4 with $\beta = 3.5°$. These tests were with three angles of attack (0°, ±5°) in air, and with five angles of attack (0°, ±5°, ±10°) in CF_4. Comparisons of these data with the data for $\beta = 0°$ are shown in figure 21 for Mach 6. Sideslip angle apparently does not have a significant effect on the longitudinal coefficients or L/D within the range of these results. The data do indicate a slight but consistent decrease in C_A with increasing β for $-5^\circ \leq \alpha \leq 5^\circ$; it is within the range of uncertainty, however. An attempt was made to measure lateral stability characteristics, but the results were inconclusive. Two factors impeded the attempt: (1) loads were small relative to the balance lateral elements, even though these elements are quite sensitive in comparison to the longitudinal elements; and (2) inertia loads imparted by the model injection system tended to shift the output of the balance lateral elements in an unpredictable way. This was particularly true for the side-mounted injection system in the Mach 10 tunnel.

Concluding Remarks

Forces, moments, and shock shapes were measured with two model sizes of the AFE configuration. Tests were conducted in two air wind tunnels at Mach numbers of 6 and 10 and in a CF_4 wind tunnel at a Mach number of 6. An inviscid-flow computer code was used to predict the aerodynamic characteristics and shock shapes at the wind-tunnel test conditions. The results lead to the following concluding remarks.

Changes in Mach number from 6 to 10 in air or in Reynolds number by a factor of 13 have little effect on the aerodynamic coefficients, shock shapes, or lift-to-drag ratio. Changes in density ratio across the normal shock from approximately 5 (air) to 12 (CF_4) have a strong effect on aerodynamic coefficients and shock detachment distance, but not on lift-to-drag ratio. The predictions are, for the most part, in very good agreement with the measurements. Tests in CF_4 provide a better simulation of predicted flight results than do tests in air. The tests in air indicate that the configuration is longitudinally stable and trimmed at an angle of attack of 3.5°. The CF_4 results indicate more stability at angles of attack less than 5° and a trim angle of -1°. The lift-to-drag ratio in air or CF_4 is 0.29 at an angle of attack of 0° and is linear with angle of attack over the range from -10° to 10°. Because trim angle is a function of density ratio, the value of lift-to-drag ratio at trim is also a function of density ratio. A variation in sideslip angle from 0° to 4° has little effect on the longitudinal aerodynamic coefficients or lift-to-drag ratio.

NASA Langley Research Center
Hampton, VA 23665-5225
September 29, 1989

References

1. Walberg, Gerald D.: A Review of Aeroassisted Orbit Transfer. AIAA-82-1378, Aug. 1982.
2. Wells, William L.: Wind-Tunnel Preflight Test Program for Aeroassist Flight Experiment. *Technical Papers—AIAA Atmospheric Flight Mechanics Conference, 1987*, pp. 151–163. (Available as AIAA-87-2367.)
3. Wells, William L.: *Free-Shear-Layer Turning Angle in Wake of Aeroassist Flight Experiment (AFE) Vehicle at Incidence in $M=10$ Air and $M=6$ CF_4*. NASA TM-100479, 1988.
4. Micol, John R.: Experimental and Predicted Pressure and Heating Distributions for an Aeroassist Flight Experiment Vehicle in Air at Mach 10. AIAA-89-1731, June 1989.
5. Wells, William L.: Measured and Predicted Aerodynamic Heating on a Cylinder in Wake of AFE Configuration at Incidence. AIAA-89-2162, Aug. 1989.
6. Micol, John R.: Simulation of Real-Gas Effects on Pressure Distributions for a Proposed Aeroassist Flight Experiment Vehicle and Comparison to Prediction. AIAA-87-2368, Aug. 1987.
7. Jones, Jim J.: The Rationale for an Aeroassist Flight Experiment. AIAA-87-1508, June 1987.
8. Walberg, G. D.; Siemers, P. M., III; Calloway, R. L.; and Jones, J. J.: The Aeroassist Flight Experiment. IAF Paper 87-197, Oct. 1987.
9. Jones, Robert A.; and Hunt, James L. (appendix A by James L. Hunt, Kathryn A. Smith, and Robert B. Reynolds and appendix B by James L. Hunt and Lillian R. Boney): *Use of Tetrafluoromethane To Simulate Real-Gas Effects on the Hypersonic Aerodynamics of Blunt Vehicles.* NASA TR R-312, 1969.
10. Cheatwood, F. McNeil; DeJarnette, Fred R.; and Hamilton, H. Harris, II: *Geometrical Description for a Proposed Aeroassist Flight Experiment Vehicle.* NASA TM-87714, 1986.
11. Miller, C. G.; and Smith, F. M.: Langley Hypersonic Facilities Complex—Description and Application. AIAA-86-0741, Mar. 1986.
12. Miller, Charles G., III; and Gnoffo, Peter A.: *Pressure Distributions and Shock Shapes for 12.84°/7° On-Axis and Bent-Nose Biconics in Air at Mach 6.* NASA TM-83222, 1981.
13. Midden, Raymond E.; and Miller, Charles G., III: *Description and Calibration of the Langley Hypersonic CF_4 Tunnel—A Facility for Simulating Low γ Flow as Occurs for a Real Gas.* NASA TP-2384, 1985.
14. Weilmuenster, K. James; and Hamilton, H. Harris, II: A Comparison of Computed and Measured Aerodynamic Characteristics of a Proposed Aeroassist Flight Experiment Configuration. AIAA-86-1366, June 1986.
15. Sutton, Kenneth: *Relations for the Thermodynamic and Transport Properties in the Testing Environment of the Langley Hypersonic CF_4 Tunnel.* NASA TM-83220, 1981.
16. Miller, Charles G., III; Micol, John R.; and Gnoffo, Peter A.: *Laminar Heat-Transfer Distributions on Biconics at Incidence in Hypersonic-Hypervelocity Flows.* NASA TP-2213, 1985.
17. Hayes, Wallace D.; and Probstein, Ronald F.: Viscous Hypersonic Similitude. IAS Rep. No. 59-63, Jan. 1959.
18. Roberts, Barney B.: Systems Analysis and Technology Development for the NASA Orbit Transfer Vehicle. AIAA-85-0965, June 1985.
19. Gamble, Joe D.; Spratlin, Kenneth M.; and Skalecki, Lisa M.: Lateral Directional Requirements for a Low L/D Aeromaneuvering Orbital Transfer Vehicle. *A Collection of Technical Papers—AIAA Atmospheric Flight Mechanics Conference*, Aug. 1984, pp. 402–413. (Available as AIAA-84-2123.)

Table I. Load Ratings for Balances Used in AFE Tests

Model size, in.	Load rating		
	Normal, lbf	Axial, lbf	Pitch, in-lbf
3.67	35	80	35
2.50	5	10	5

Table II. Nominal Test Conditions

Re_∞, ft^{-1}	p_t, lbf/in^2	T_t, °R	p_∞, lbf/in^2	T_∞, °R	M_∞	U_∞, ft/sec	q_∞, lbf/in^2	ρ_2/ρ_∞	Re_2, ft^{-1}	$p_{t,2}$, lb/in^2	$T_{t,2}$, °R	γ_2
Langley 20-Inch Mach 6 Tunnel; air test gas												
0.63×10^6	30	845	0.023	108.3	5.84	2975	0.54	5.2	1.00×10^5	1.00	845	1.40
2.21×10^6	126	910	.084	112.5	5.94	3095	2.10	5.2	3.52×10^5	3.86	910	1.40
Langley Hypersonic CF_4 Tunnel; CF_4 test gas												
0.30×10^6	970	1160	0.026	300	6.24	2850	0.63	11.8	0.97×10^6	1.23	1150	1.11
$.46 \times 10^6$	1500	1160	.039	292	6.29	2844	.95	11.7	1.48×10^6	1.86	1150	1.11
Langley 31-Inch Mach 10 Tunnel; air test gas												
0.25×10^6	150	1800	0.0045	97.4	9.55	4624	0.29	6.0	0.211×10^6	0.54	1800	1.34
$.54 \times 10^6$	350	1835	.0095	96.9	9.74	4679	.63	6.0	$.447 \times 10^6$	1.17	1835	1.34
1.09×10^6	700	1810	.0175	91.7	9.90	4651	1.20	6.0	$.866 \times 10^6$	2.23	1810	1.34
2.10×10^6	1450	1830	.0324	90.5	10.05	4689	2.29	6.0	1.626×10^6	4.25	1830	1.34

Table III. Balance-Related Uncertainties in Experimental Longitudinal Aerodynamic Coefficients

$Re_{2,d}$	d, in.	Uncertainty		
		$\Delta C_A, \pm$	$\Delta C_N, \pm$	$\Delta C_m, \pm$
Mach 10 air				
4,030	2.50	0.0357	0.0180	0.0136
9,900	2.50	.0163	.0081	.0062
17,660	2.50	.0085	.0043	.0032
49,830	3.67	.0165	.0072	.0040
Mach 6 air				
51,470	3.67	0.0180	0.0079	0.0042
30,420	3.67	.0725	.0317	.0170
Mach 6 CF_4				
45,260	3.67	0.0401	0.0176	0.0094
30,830	2.50	.0106	.0053	.0040

Table IV. Measured Aerodynamic Coefficients in Air at Mach 9.55

[$\mathrm{Re}_\infty = 0.23 \times 10^6$/ft; $\mathrm{Re}_{2,d} = 4.03 \times 10^3$; $d = 2.50$ in.; and $\beta = 0°$]

α, deg	q_∞, psi	C_A	C_N	C_m	L/D
−9.9	0.280	1.176	0.279	0.0233	0.430
−8.0	.280	1.230	.310	.0177	.406
−5.9	.281	1.275	.331	.0196	.373
−4.9	.283	1.286	.340	.0165	.358
−3.9	.284	1.307	.348	.0182	.340
−1.9	.284	1.323	.351	.0131	.302
.2	.285	1.346	.400	.0077	.294
2.1	.285	1.349	.399	.0014	.257
4.0	.285	1.364	.412	.0002	.227
5.2	.284	1.360	.418	−.0064	.211
6.1	.284	1.365	.430	−.0087	.201
8.2	.284	1.368	.438	−.0152	.169
10.1	.284	1.382	.443	−.0159	.134

Table V. Measured Aerodynamic Coefficients in Air at Mach 9.74

[$\mathrm{Re}_\infty = 0.57 \times 10^6$/ft; $\mathrm{Re}_{2,d} = 9.90 \times 10^3$; $d = 2.50$ in.; and $\beta = 0°$]

α, deg	q_∞, psi	C_A	C_N	C_m	L/D
−9.9	0.634	1.167	0.284	0.0231	0.437
−7.9	.631	1.211	.311	.0189	.409
−5.9	.627	1.253	.330	.0170	.376
−4.8	.622	1.265	.338	.0159	.359
−3.8	.624	1.279	.347	.0145	.345
−1.8	.624	1.293	.365	.0095	.317
.2	.625	1.307	.381	.0064	.287
2.2	.625	1.321	.387	.0042	.252
4.3	.626	1.329	.402	−.0011	.223
5.2	.628	1.337	.404	−.0026	.205
6.2	.628	1.336	.413	−.0062	.194
8.3	.628	1.344	.421	−.0098	.160
10.3	.627	1.345	.431	−.0153	.131

Table VI. Measured Aerodynamic Coefficients in Air at Mach 9.90

[$\mathrm{Re}_\infty = 1.04 \times 10^6$/ft; $\mathrm{Re}_{2,d} = 17.66 \times 10^3$; $d = 2.50$ in.; and $\beta = 0°$]

α, deg	q_∞, psi	C_A	C_N	C_m	L/D
−9.8	1.191	1.189	0.284	0.0233	0.430
−7.7	1.191	1.237	.312	.0198	.401
−5.6	1.191	1.268	.334	.0160	.370
−4.7	1.193	1.285	.338	.0161	.353
−3.6	1.192	1.296	.352	.0137	.341
−1.7	1.194	1.315	.365	.0112	.309
0.4	1.192	1.332	.375	.0092	.274
2.3	1.191	1.340	.390	.0051	.248
4.5	1.193	1.348	.401	.0006	.215
5.4	1.194	1.359	.408	−.0001	.200
6.3	1.194	1.355	.407	−.0036	.183
8.5	1.192	1.358	.424	−.0096	.156
10.5	1.193	1.359	.435	−.0157	.128

Table VII. Measured Aerodynamic Coefficients in Air at Mach 10.05

[$\mathrm{Re}_\infty = 2.13 \times 10^6$/ft; $\mathrm{Re}_{2,d} = 49.83 \times 10^3$; $d = 3.67$ in.; and $\beta = 0°$]

α, deg	q_∞, psi	C_A	C_N	C_m	L/D
−9.9	2.26	1.188	0.289	0.0226	0.436
−7.9	2.27	1.222	.308	.0194	.404
−5.9	2.28	1.256	.328	.0165	.374
−4.8	2.28	1.275	.338	.0142	.358
−3.8	2.29	1.283	.344	.0142	.341
−1.8	2.29	1.303	.360	.0119	.311
0.4	2.29	1.317	.376	.0085	.279
2.2	2.29	1.328	.386	.0047	.250
4.2	2.29	1.336	.399	−.0002	.221
5.2	2.29	1.342	.404	−.0033	.204
6.2	2.29	1.345	.411	−.0058	.191
8.2	2.29	1.345	.421	−.0114	.162
10.2	2.30	1.344	.432	−.0176	.135

Table VIII. Measured Aerodynamic Coefficients in Air at Mach 5.94

[$\mathrm{Re}_\infty = 0.62 \times 10^6/\mathrm{ft}$; $\mathrm{Re}_{2,d} = 30.42 \times 10^3$; $d = 3.67$ in.; and $\beta = 0°$]

α, deg	q_∞, psi	C_A	C_N	C_m	L/D
−10.1	0.534	1.201	0.292	0.0256	0.440
−7.0	.477	1.258	.326	.0204	.395
−5.1	.534	1.282	.342	.0164	.363
−2.9	.529	1.303	.357	.0138	.329
0	.521	1.327	.377	.0081	.285
3.0	.474	1.351	.397	.0026	.238
5.1	.519	1.353	.407	−.0027	.207
7.1	.531	1.359	.418	−.0075	.177
10.1	.485	1.368	.434	−.0152	.132

Table IX. Measured Aerodynamic Coefficients in Air at Mach 5.94

[$\mathrm{Re}_\infty = 2.20 \times 10^6/\mathrm{ft}$; $\mathrm{Re}_{2,d} = 106.51 \times 10^3$; $d = 3.67$ in.; and $\beta = 0°$]

α, deg	q_∞, psi	C_A	C_N	C_m	L/D
−9.9	2.088	1.206	0.297	0.0234	0.440
−7.3	2.108	1.244	.322	.0182	.401
−5.0	2.058	1.281	.344	.0149	.365
−2.9	2.099	1.296	.357	.0117	.332
.2	2.039	1.327	.380	.0066	.283
2.9	2.093	1.336	.394	.0012	.241
5.2	2.079	1.353	.409	−.0038	.206
7.2	2.087	1.350	.417	−.0085	.176
10.2	2.060	1.362	.434	−.0163	.131

Table X. Measured Aerodynamic Coefficients in CF_4 at Mach 6.28

[$\mathrm{Re}_\infty = 0.46 \times 10^6/\mathrm{ft}$; $\mathrm{Re}_{2,d} = 45.26 \times 10^3$; $d = 3.67$ in.; and $\beta = 0°$]

α, deg	q_∞, psi	C_A	C_N	C_m	L/D
Afterbody attached					
−9.89	0.95	1.214	0.276	0.0303	0.418
−5.06	.94	1.315	.340	.0145	.355
−2.25	.94	1.366	.374	.0054	.317
.01	.92	1.401	.398	−.0015	.284
1.96	.94	1.429	.418	−.0073	.256
5.16	.94	1.455	.442	−.0141	.208
9.94	.96	1.452	.464	−.0216	.137
Afterbody detached					
−10.3	0.95	1.217	0.279	0.0286	0.429
−5.1	.96	1.318	.341	.0135	.356
−2.1	.94	1.367	.372	.0056	.313
−.2	.95	1.402	.395	−.0008	.286
5.1	.94	1.456	.443	−.0155	.209
10.0	.94	1.468	.466	−.0230	.133

Table XI. Measured Aerodynamic Coefficients in CF_4 at Mach 6.10

[$\mathrm{Re}_\infty = 0.46 \times 10^6/\mathrm{ft}$; $\mathrm{Re}_{2,d} = 30.83 \times 10^3$; $d = 2.50$ in.; and $\beta = 0°$]

α, deg	q_∞, psi	C_A	C_N	C_m	L/D
−10.0	0.971	1.212	0.286	0.0265	0.429
−4.9	.960	1.307	.345	.0123	.358
−2.0	.960	1.356	.378	.0031	.316
−.1	.960	1.382	.397	−.0025	.289
2.0	.960	1.409	.416	−.0079	.258
5.2	.970	1.435	.440	−.0145	.210
10.0	.940	1.432	.462	−.0229	.139

Table XII. Measured Aerodynamic Coefficients in Air at Mach 9.74

[$\mathrm{Re}_\infty = 0.53 \times 10^6/\mathrm{ft}$; $\mathrm{Re}_{2,d} = 9.20 \times 10^3$; $d = 2.50$ in.; and variable β]

β, deg	q_∞, psi	C_A	C_N	C_m	L/D
$\alpha = -4.75°$					
0.0	0.634	1.258	0.329	0.0148	0.352
2.0	.630	1.258	.336	.0141	.359
4.0	.624	1.257	.335	.0143	.358
$\alpha = 0.27°$					
0.0	0.622	1.318	0.373	0.0104	0.279
2.0	.625	1.317	.368	.0102	.275
4.0	.628	1.303	.380	.0058	.287
$\alpha = 5.29°$					
0.0	0.628	1.339	0.402	−0.0009	0.202
1.9	.627	1.337	.400	−.0004	.201
4.0	.629	1.333	.401	−.0019	.202

Table XIII. Measured Aerodynamic Coefficients in Air at Mach 9.90

[$\mathrm{Re}_\infty = 1.05 \times 10^6/\mathrm{ft}$; $\mathrm{Re}_{2,d} = 17.83 \times 10^3$; $d = 2.50$ in.; and variable β]

β, deg	q_∞, psi	C_A	C_N	C_m	L/D
$\alpha = -4.67°$					
0.0	1.182	1.277	0.354	0.0139	0.367
2.0	1.185	1.274	.339	.0141	.355
4.1	1.194	1.274	.340	.0149	.357
$\alpha = 0.40°$					
0.1	1.194	1.326	0.376	0.0084	0.276
2.0	1.197	1.322	.376	.0085	.277
4.1	1.193	1.326	.375	.0091	.275
$\alpha = 5.50°$					
0.1	1.196	1.355	0.406	−0.0008	0.198
2.1	1.196	1.351	.407	−.0015	.199
4.1	1.197	1.352	.404	−.0011	.197

Table XIV. Measured Aerodynamic Coefficients in Air at Mach 5.84

[$\mathrm{Re}_\infty = 0.63 \times 10^6/\mathrm{ft}$; $\mathrm{Re}_{2,d} = 29.36 \times 10^3$; $d = 3.67$ in.; and variable β]

β, deg	q_∞, psi	C_A	C_N	C_m	L/D
$\alpha = -5.1°$					
0.0	0.555	1.280	0.343	0.0169	0.365
−2.0	.534	1.298	.343	.0165	.362
−4.0	.540	1.285	.341	.0165	.363
$\alpha = -0.1°$					
0.0	0.543	1.311	0.379	0.0079	0.290
−2.0	.531	1.335	.379	.0076	.285
−4.0	.535	1.320	.377	.0078	.287
$\alpha = 5.3°$					
0.0	0.533	1.363	0.409	−0.0031	0.202
−2.0	.540	1.355	.409	−.0033	.204
−4.0	.546	1.346	.408	−.0035	.205

Table XV. Measured Aerodynamic Coefficients in Air at Mach 5.94

[$\mathrm{Re}_\infty = 2.21 \times 10^6/\mathrm{ft}$; $\mathrm{Re}_{2,d} = 106.99 \times 10^3$; $d = 3.67$ in.; and variable β]

β, deg	q_∞, psi	C_A	C_N	C_m	L/D
$\alpha = -5.0°$					
0.0	2.107	1.286	0.344	0.0146	0.363
−2.0	2.123	1.280	.343	.0146	.363
−4.0	2.131	1.270	.340	.0147	.363
$\alpha = 0.0°$					
0.0	2.064	1.334	0.380	0.0066	0.284
−2.0	2.156	1.323	.377	.0067	.284
−4.0	2.136	1.312	.375	.0065	.285
$\alpha = 5.3°$					
0.0	2.089	1.352	0.409	−0.004	0.205
−2.0	2.108	1.345	.407	−.0039	.205
−4.0	2.112	1.336	.406	−.0042	.206

Table XVI. Measured Aerodynamic Coefficients in CF_4 at Mach 6.29

[$\mathrm{Re}_{\infty} = 0.45 \times 10^6/\mathrm{ft}$; $\mathrm{Re}_{2,d} = 44.19 \times 10^3$; $d = 3.67$ in.; and $\beta = 3.5°$]

α, deg	q_{∞}, psi	C_A	C_N	C_m	L/D
−9.9	0.970	1.216	0.277	0.0297	0.419
−5.1	.910	1.310	.336	.0157	.354
−.1	.950	1.386	.392	−.0001	.284
5.0	.940	1.438	.437	−.0129	.211
10.0	.950	1.447	.463	−.0214	.137

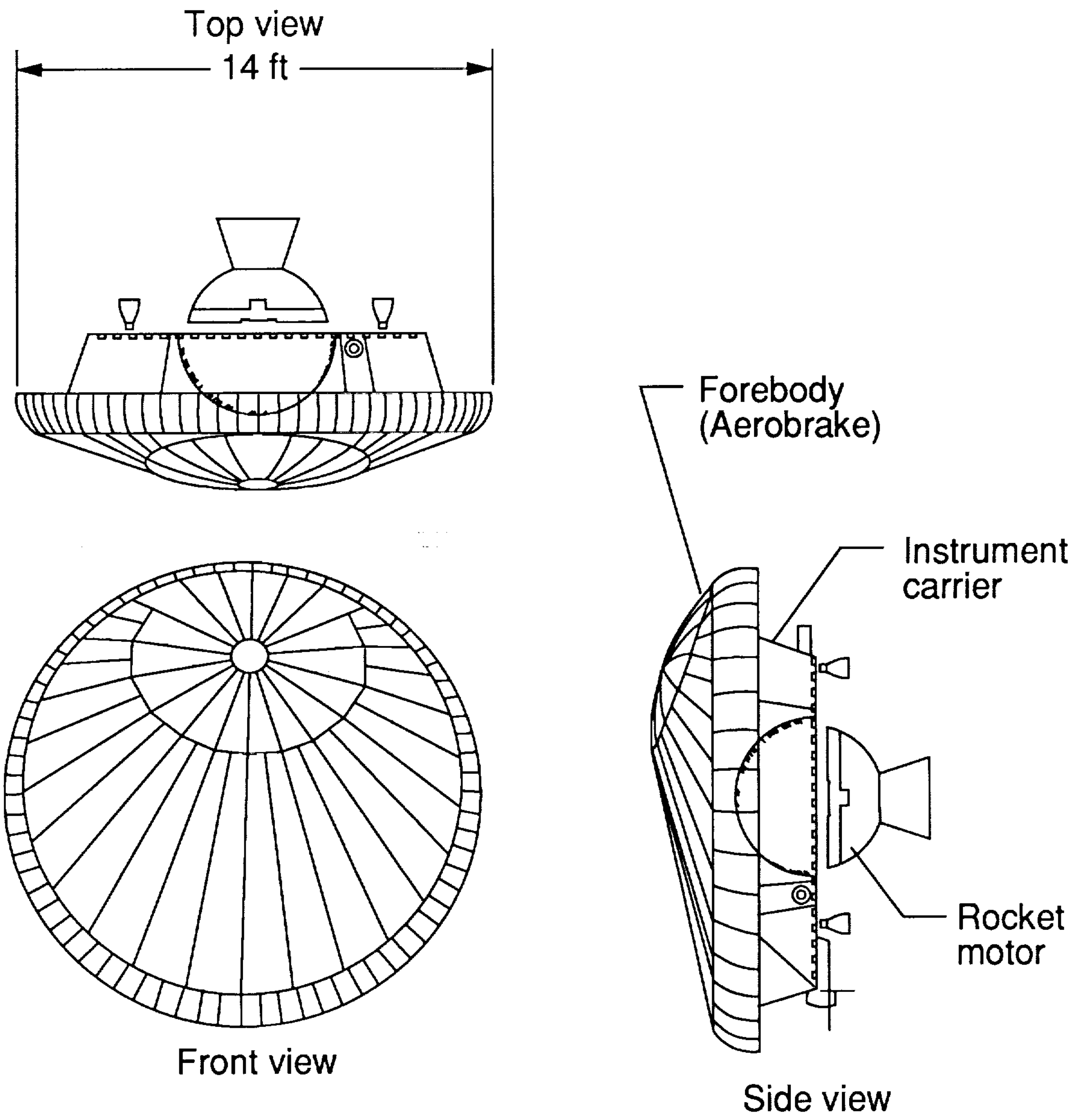

Figure 1. Sketch of AFE flight vehicle configuration.

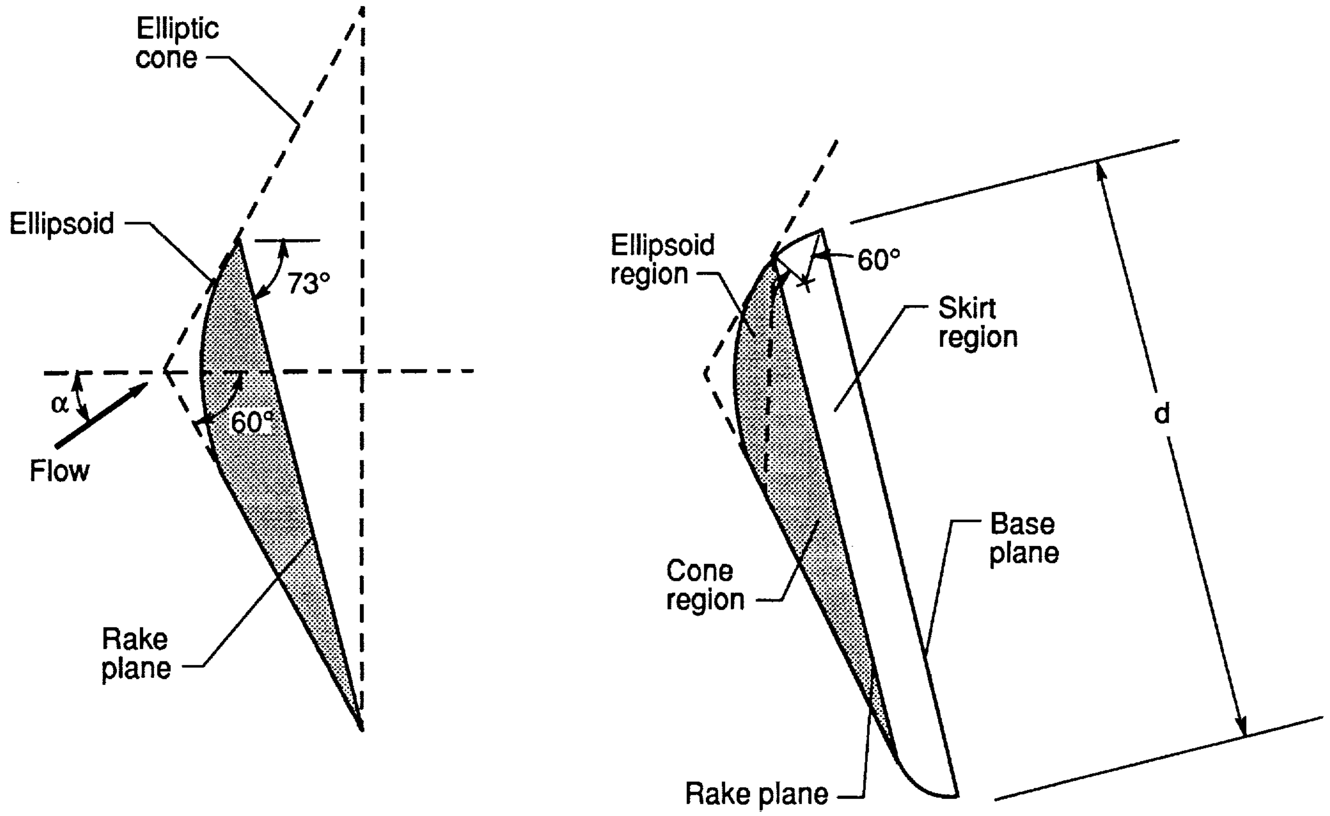

Figure 2. Development of AFE configuration from original elliptic cone. Symmetry plane shown.

ORIGINAL PAGE
BLACK AND WHITE PHOTOGRAPH

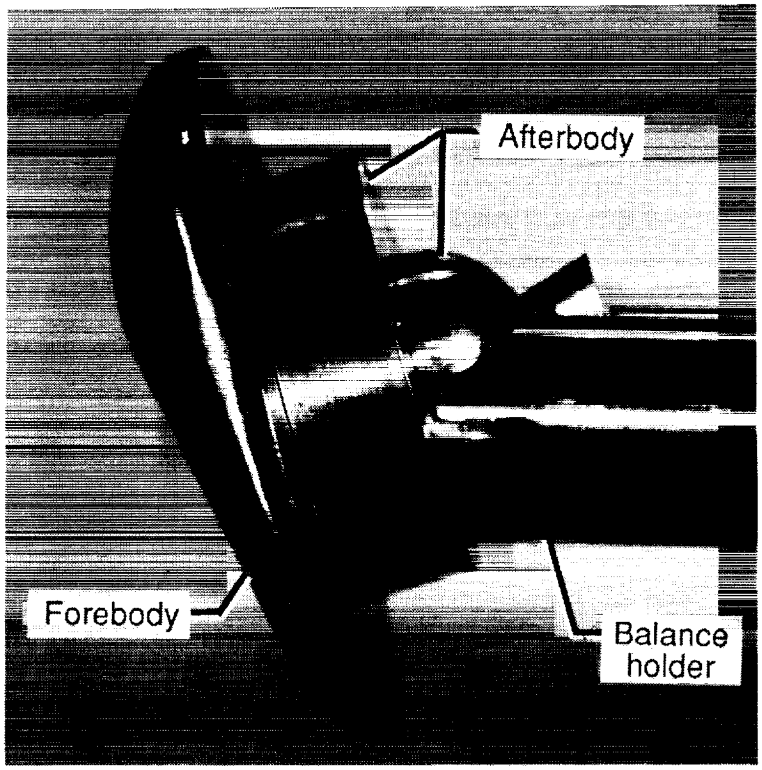

(a) Photograph.

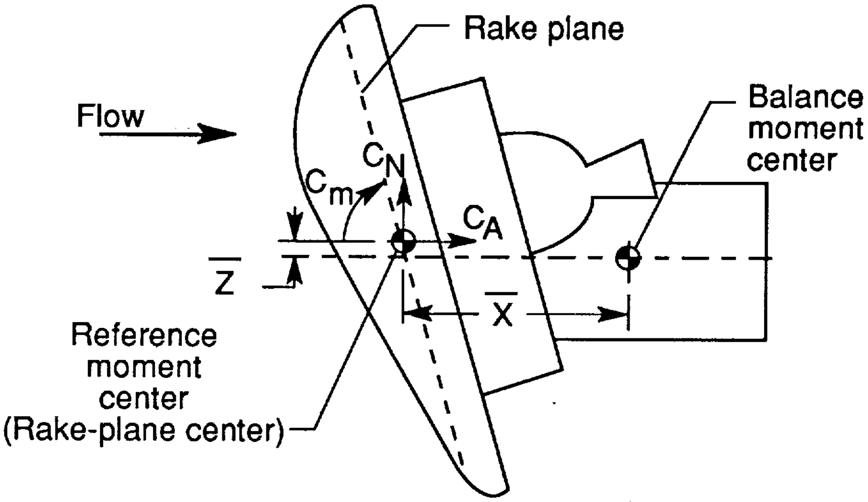

(b) Sketch with reference moment center and transfer distances $\overline{X}$ and $\overline{Z}$ identified.

Figure 3. AFE force-and-moment wind-tunnel model. $\alpha = 0°$.

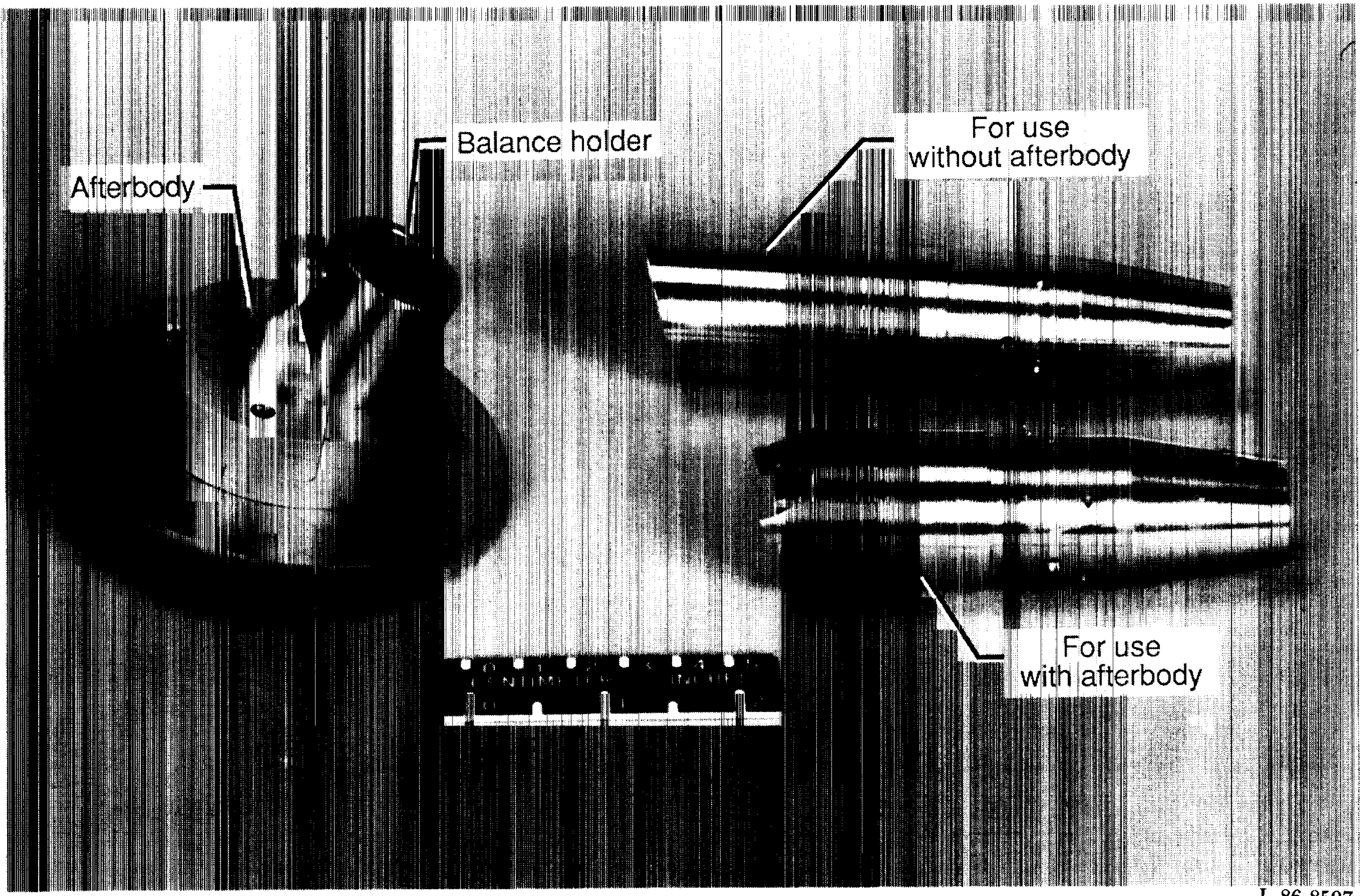

L-86-8597

Figure 4. Photograph of AFE wind-tunnel model (oblique aft view) with two balance shrouds.

ORIGINAL PAGE
BLACK AND WHITE PHOTOGRAPH

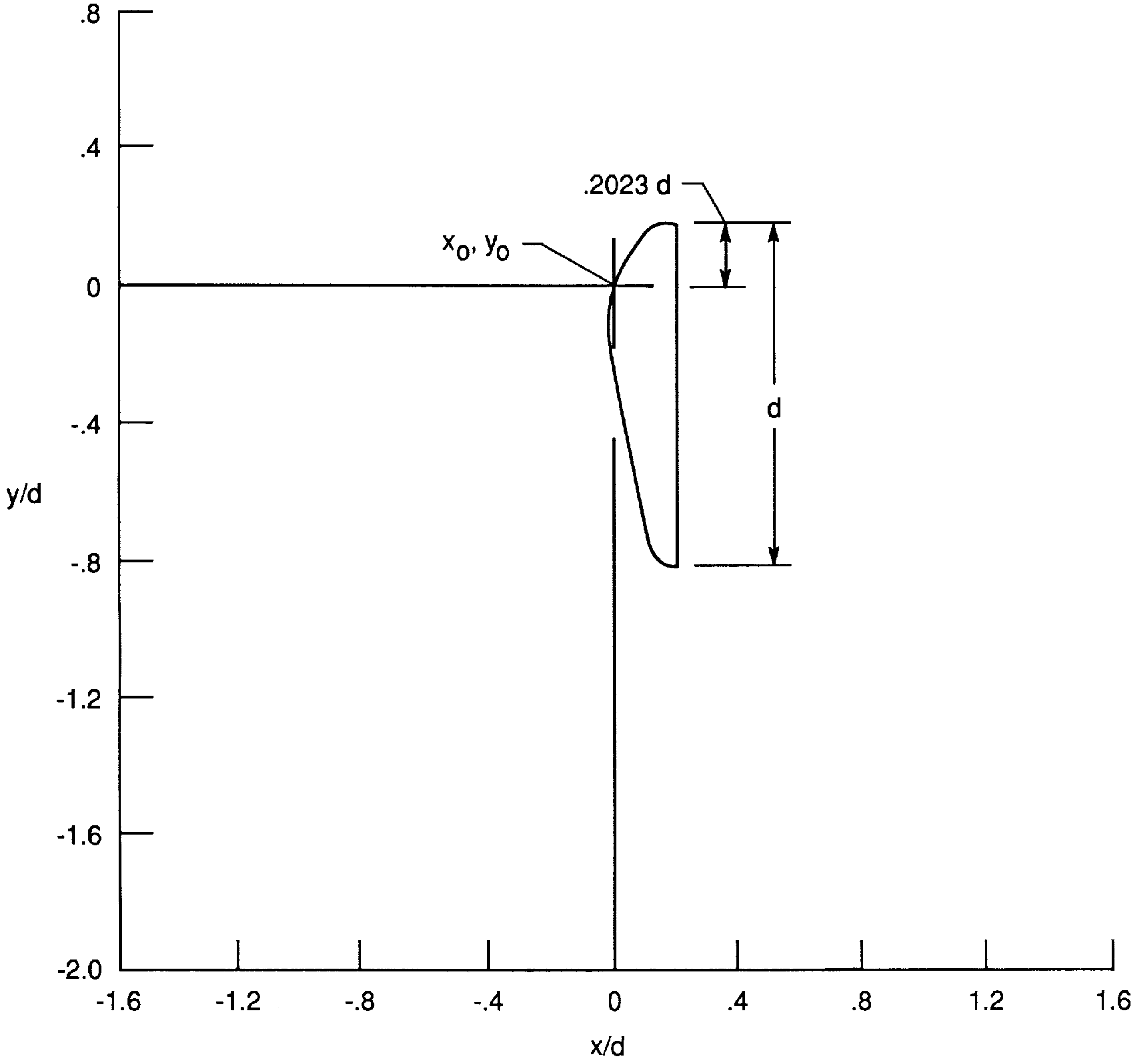

Figure 5. Coordinate system for shock shape display.

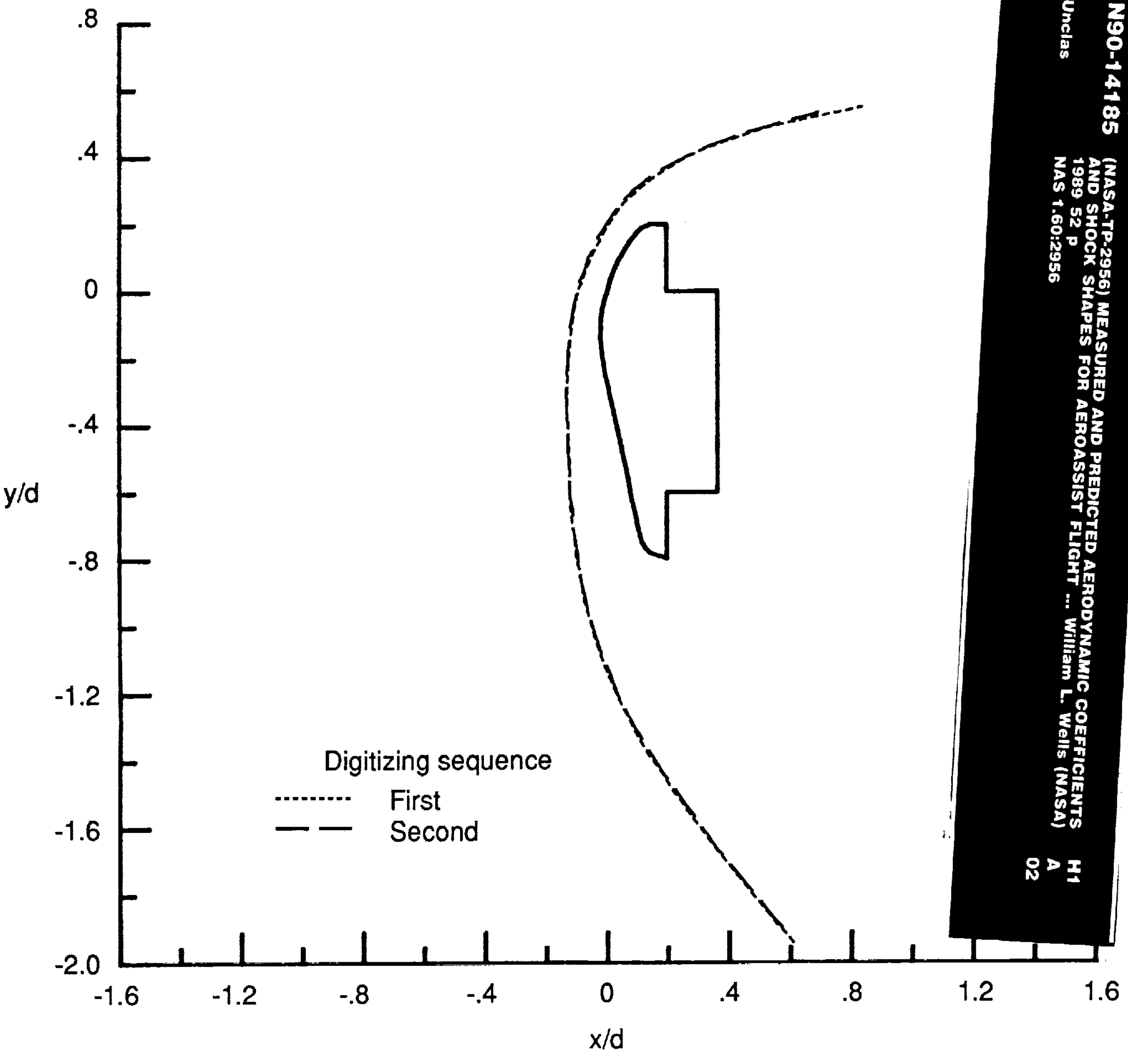

Figure 6. Indication of accuracy due to digitizing process in Langley 20-Inch Mach 6 Tunnel. $\alpha = 0^\circ$; $\mathrm{Re}_\infty = 0.6 \times 10^6/\mathrm{ft}$ in air.

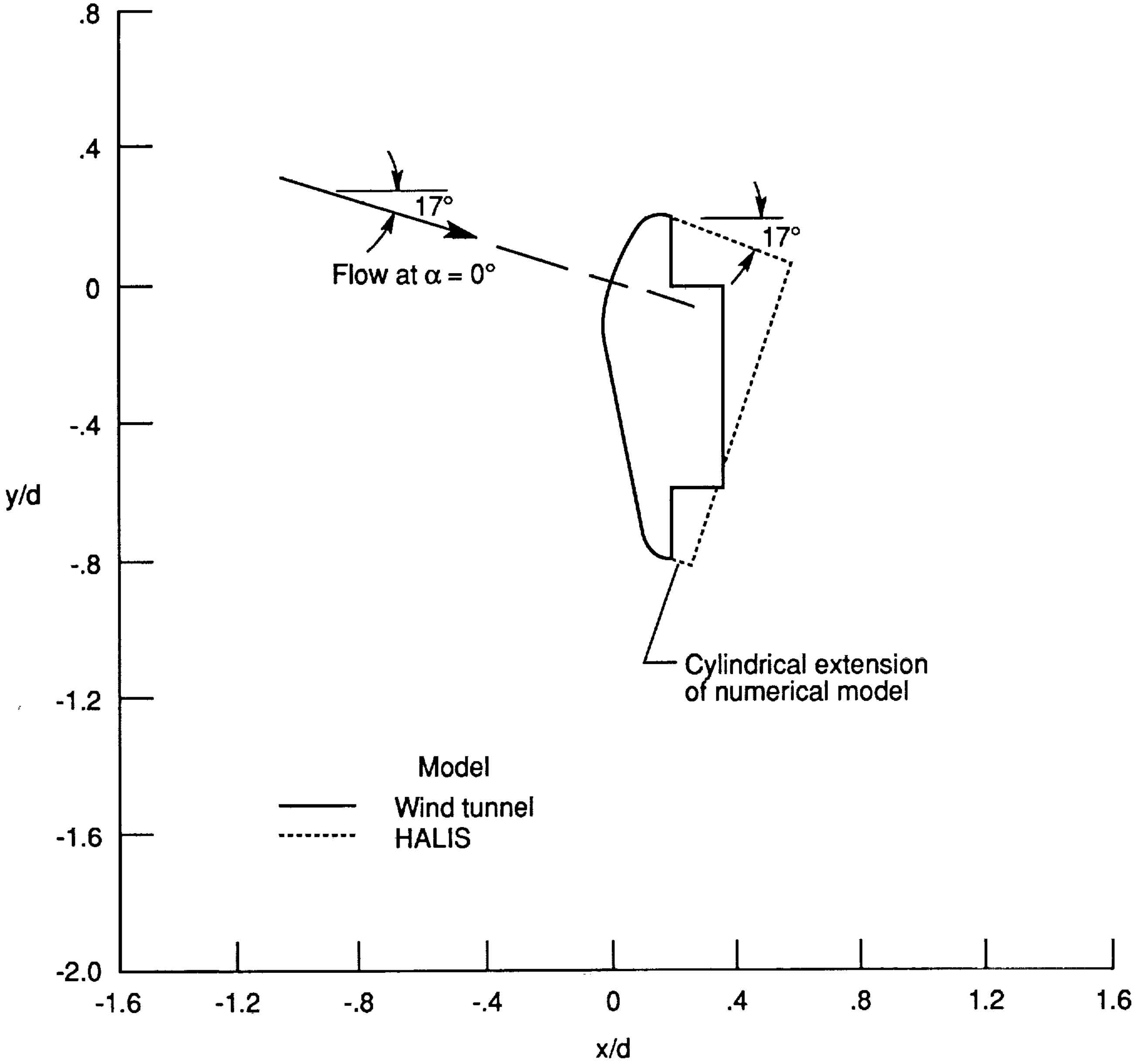

Figure 7. Comparison of digitized shape of wind-tunnel model and numerical model.

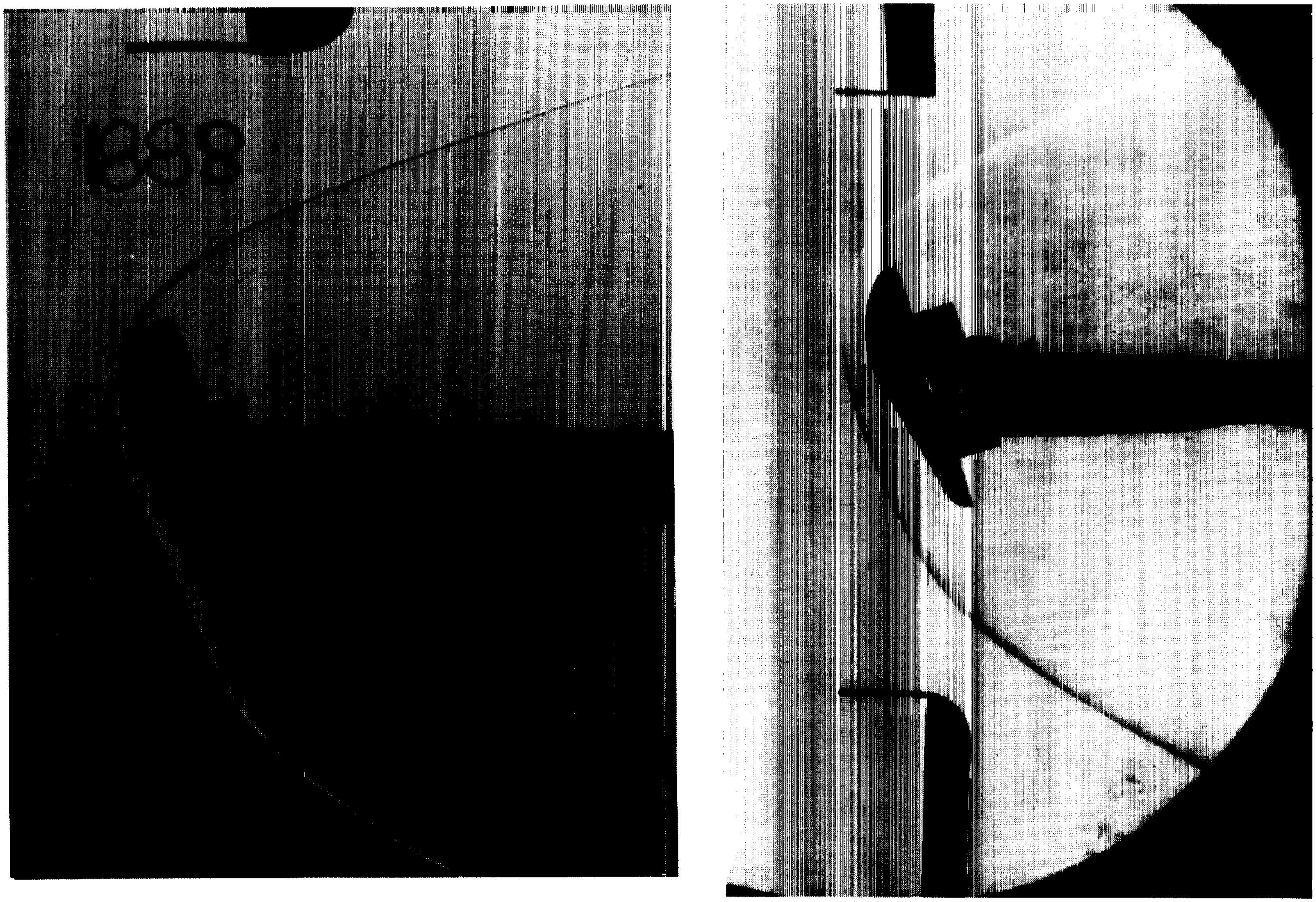

(a) CF_4 test gas; $\rho_2/\rho_\infty = 11.7$.

(b) Air test gas; $\rho_2/\rho_\infty = 5.2$.

Figure 8. Typical schlieren photographs for AFE at Mach 6 and $\alpha = 0$.

ORIGINAL PAGE
BLACK AND WHITE PHOTOGRAPH

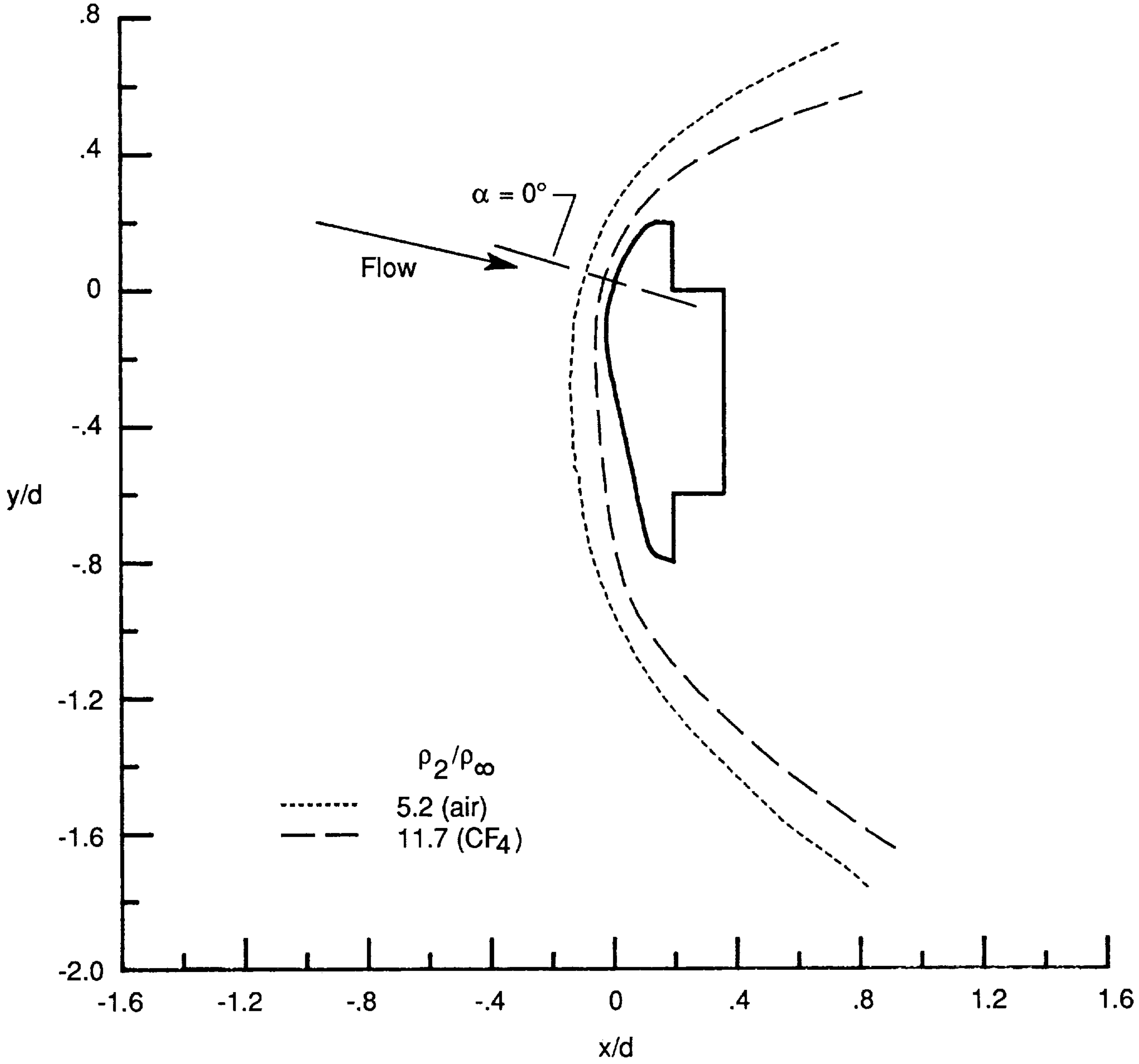

(a) $\alpha = 10^{\circ}$.

Figure 9. Effect of ρ_2/ρ_∞ on AFE shock shapes and detachment distances at Mach 6.

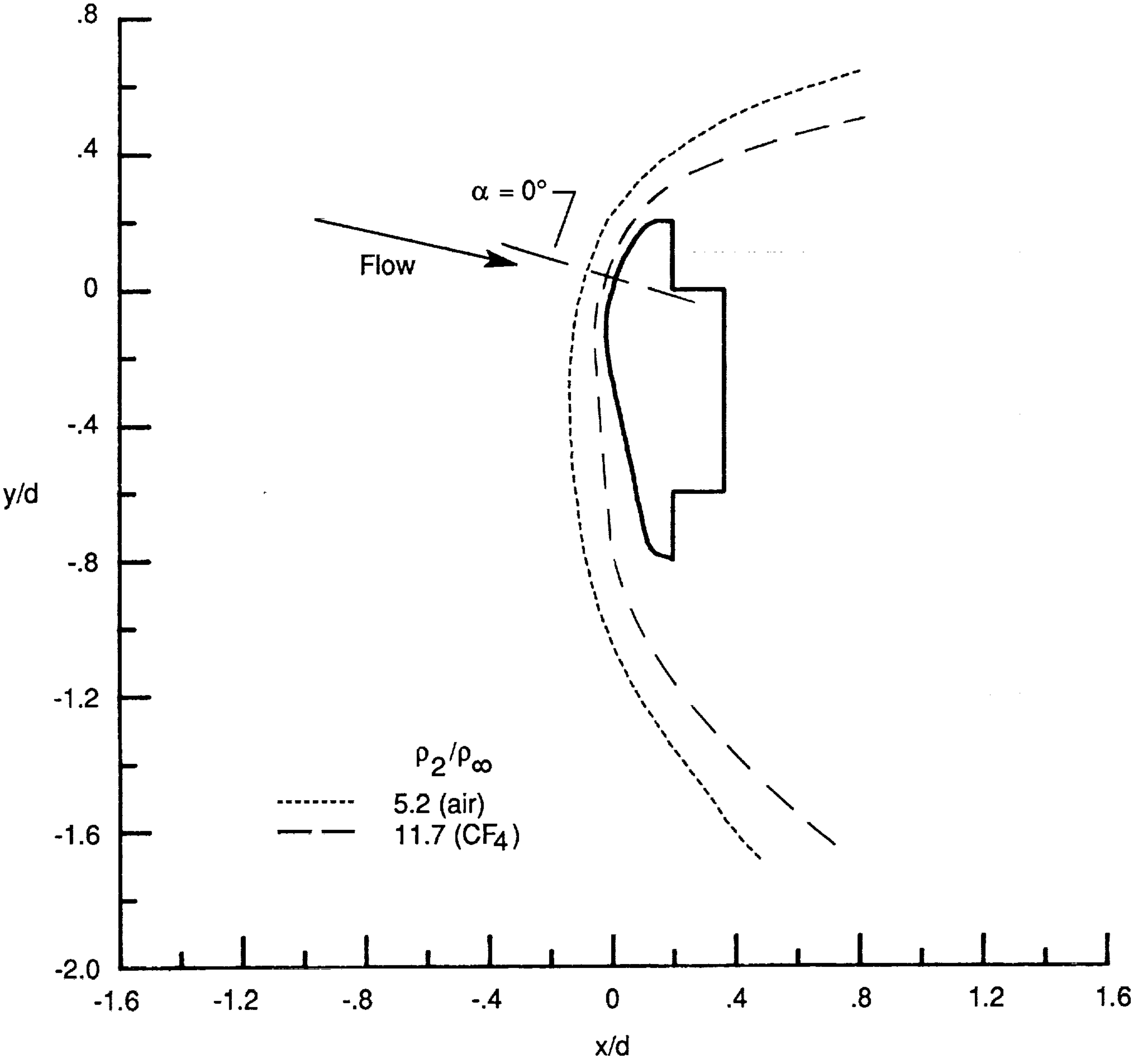

(b) $\alpha = 5°$.

Figure 9. Continued.

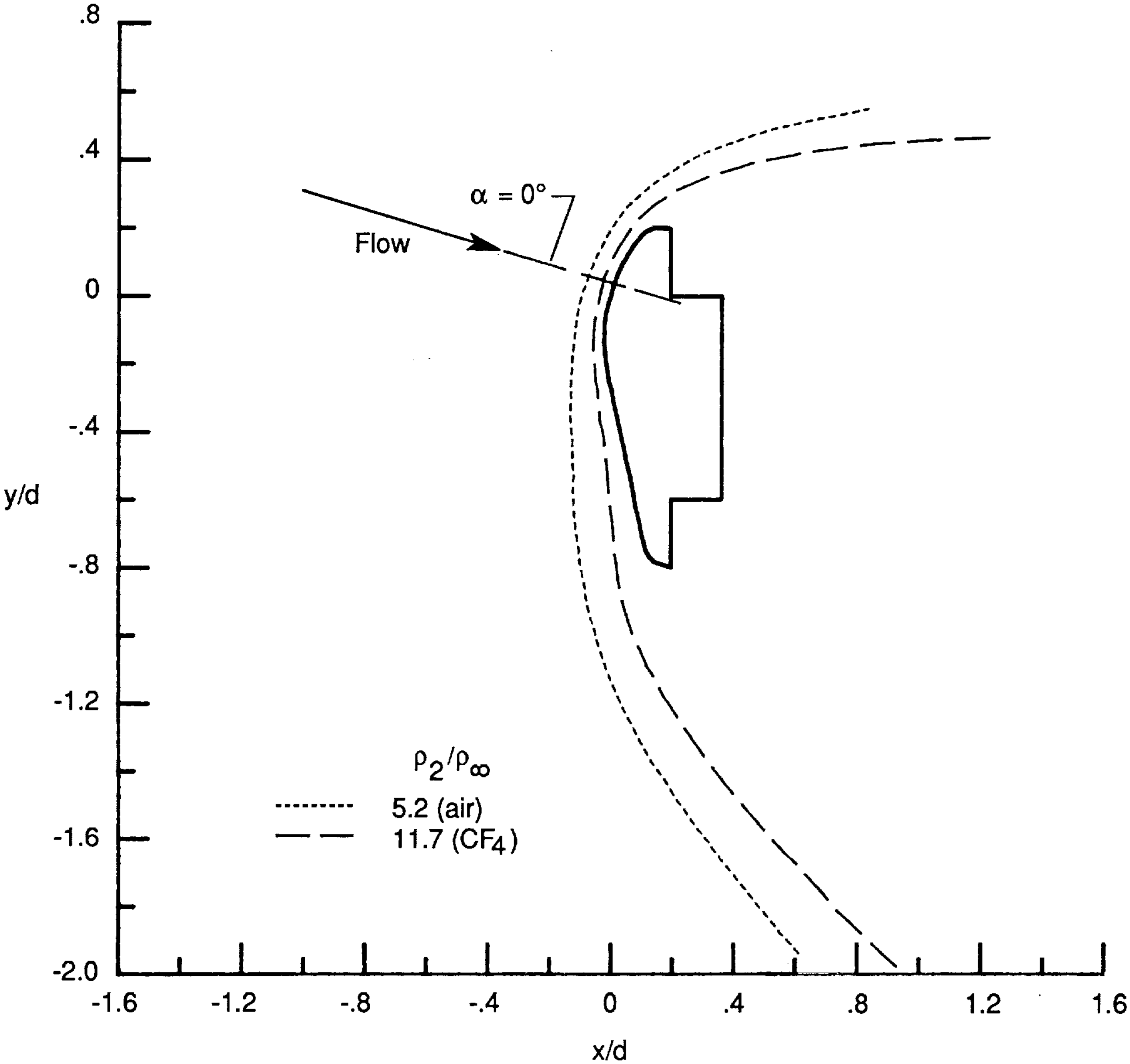

(c) $\alpha = 0°$.

Figure 9. Continued.

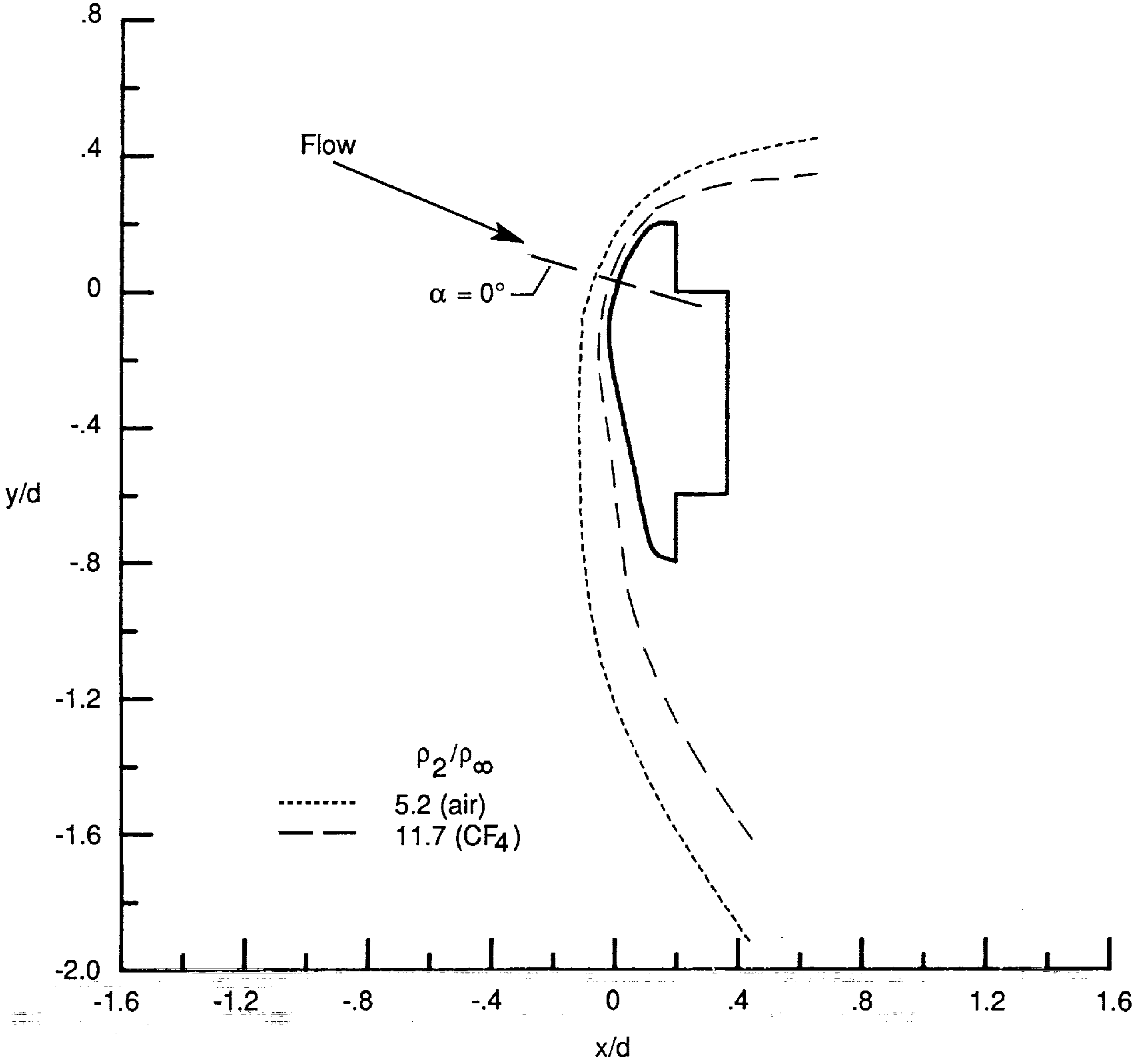

(d) $\alpha = -5°$.

Figure 9. Continued.

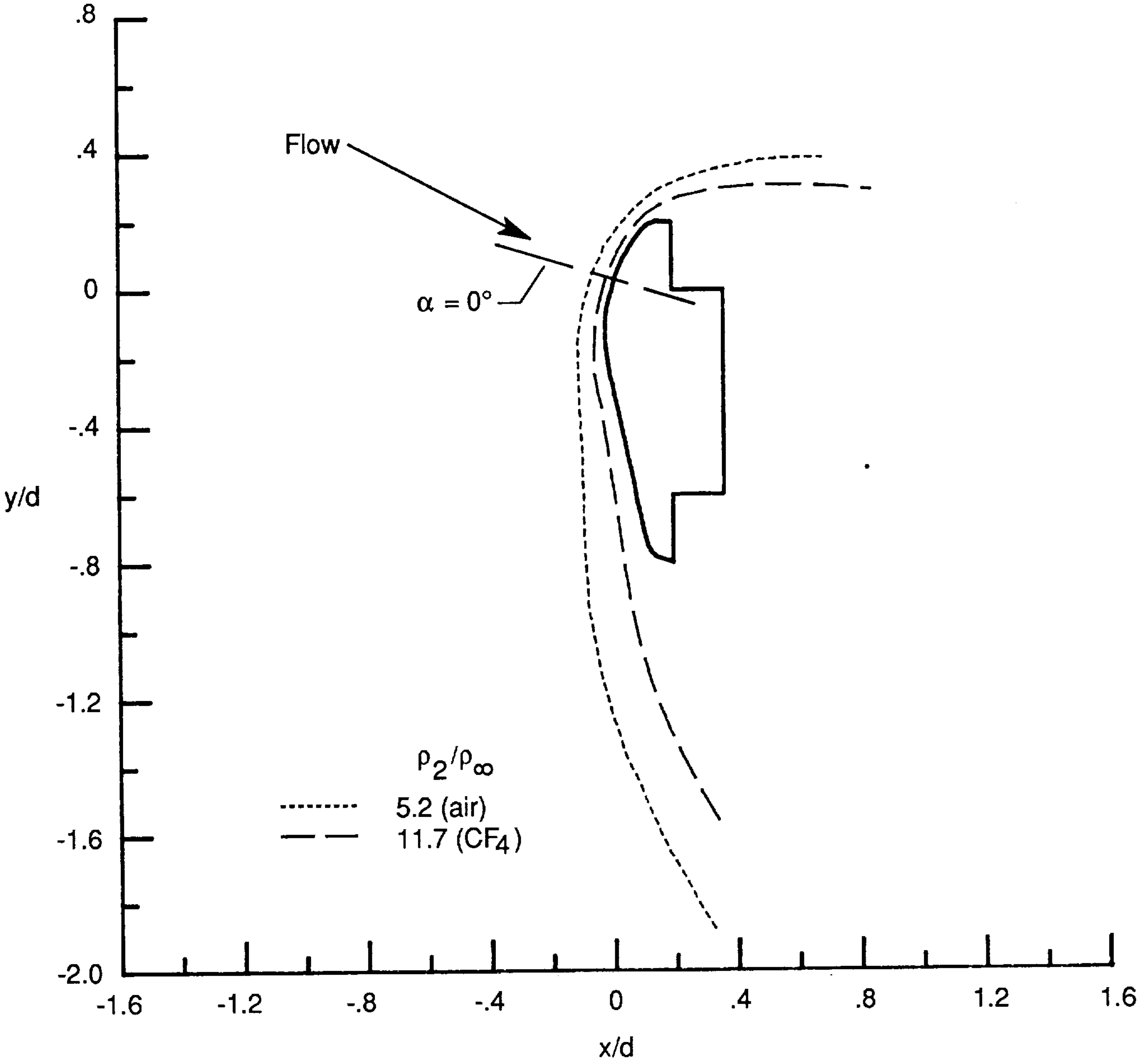

(e) $\alpha = -10°$.

Figure 9. Concluded.

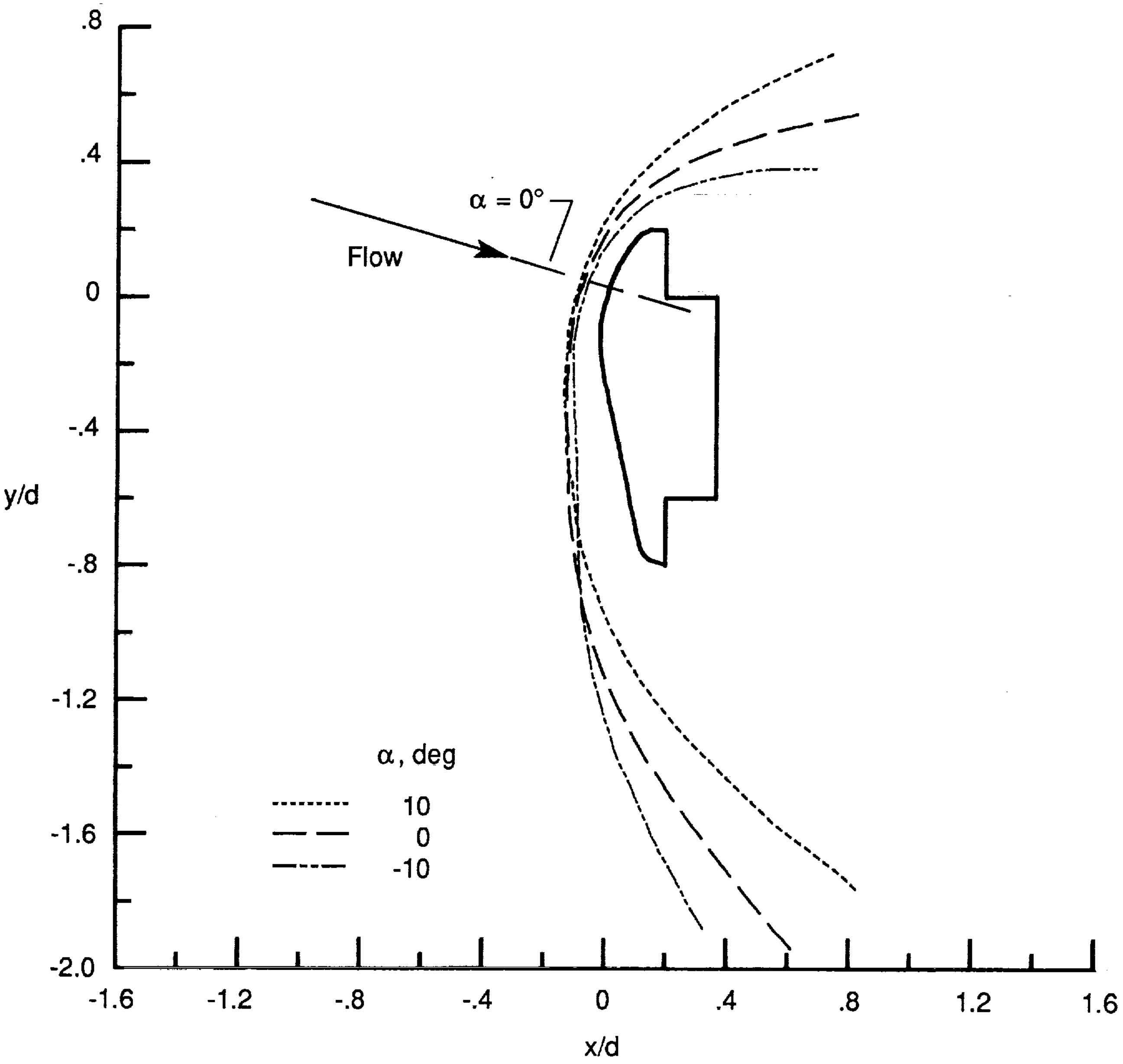

Figure 10. Effect of α in Mach 6 air.

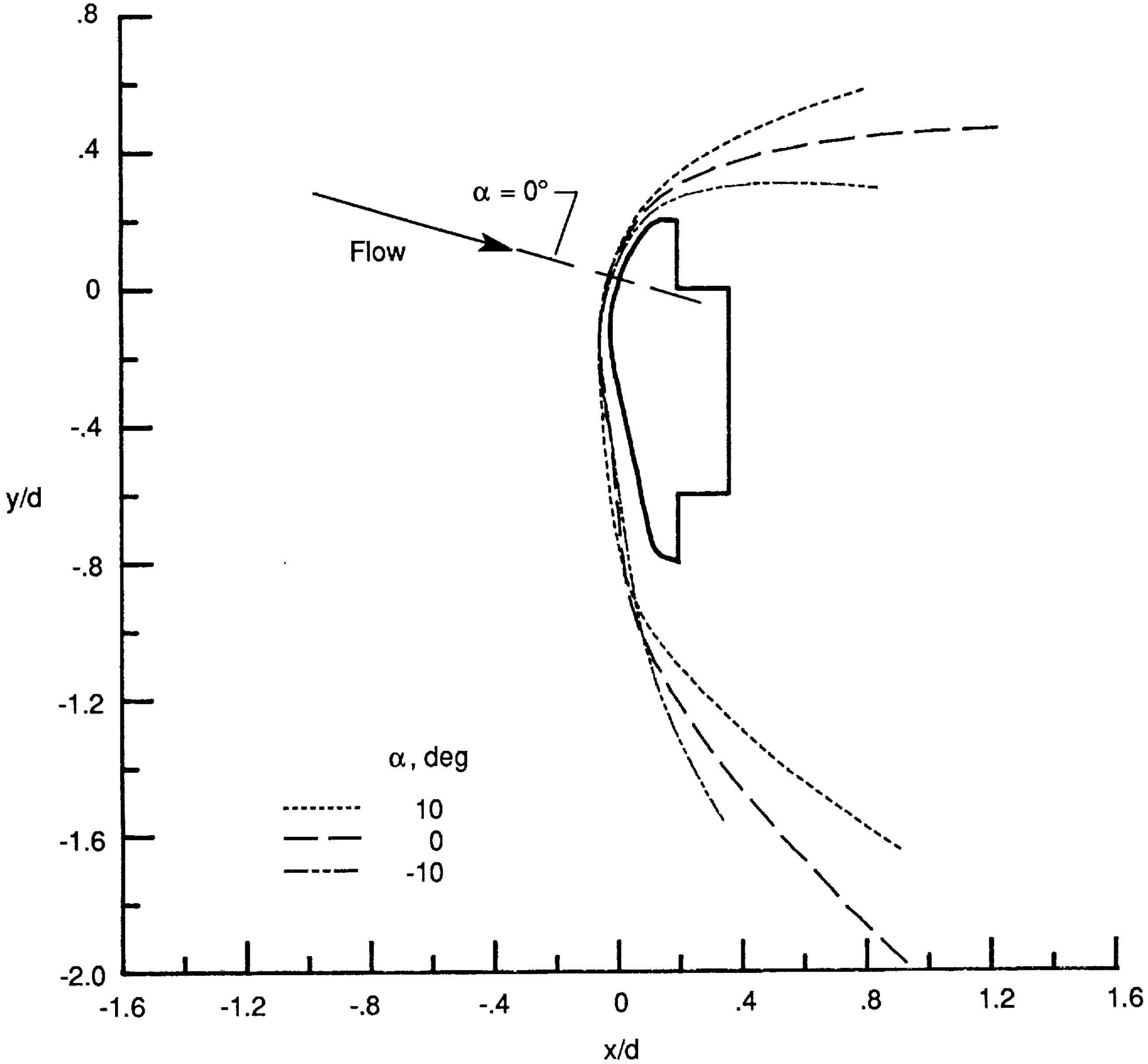

Figure 11. Effect of α in Mach 6 CF_4.

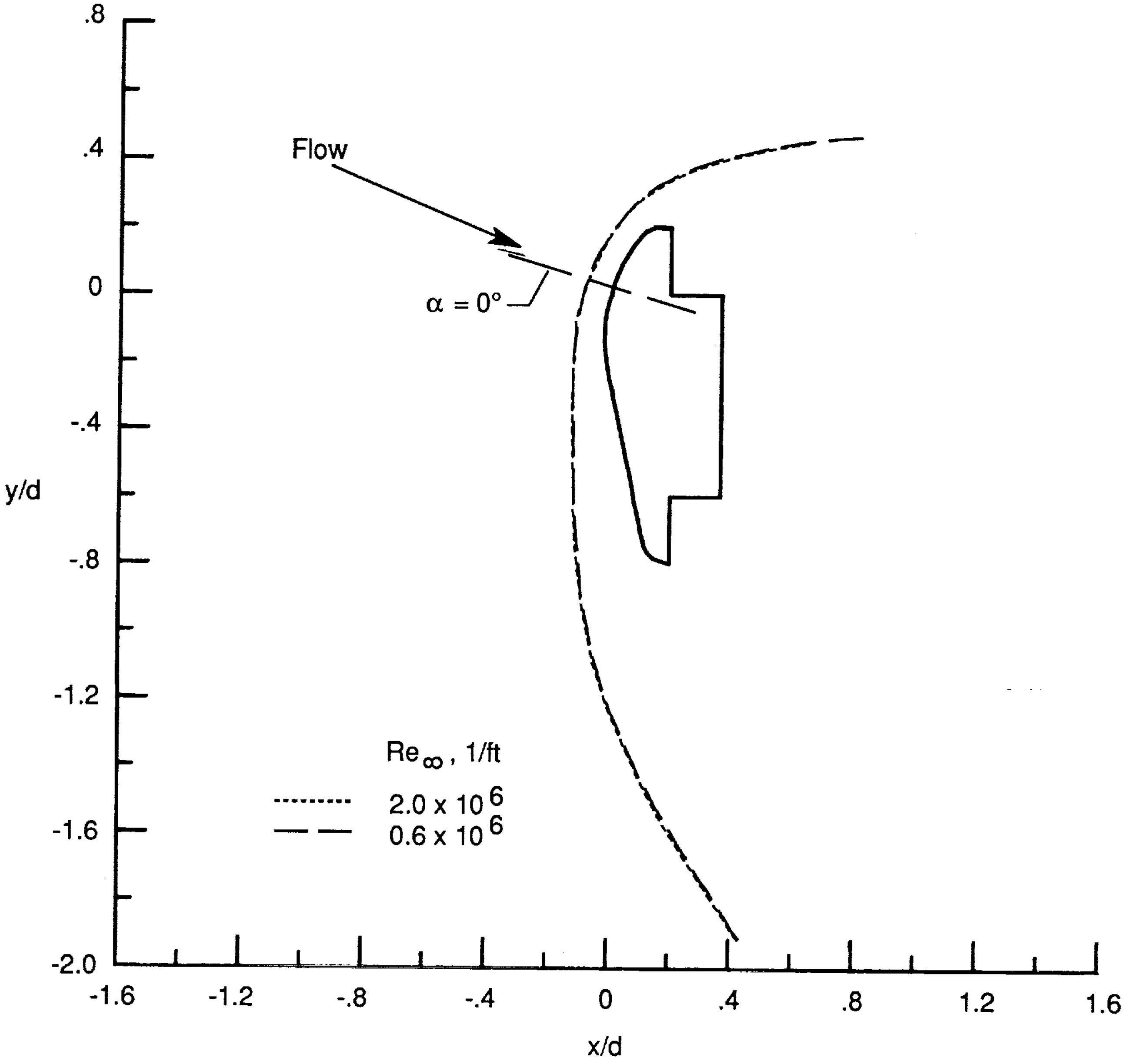

Figure 12. Effect of Re_∞ for $\alpha = -5°$ in Mach 6 air.

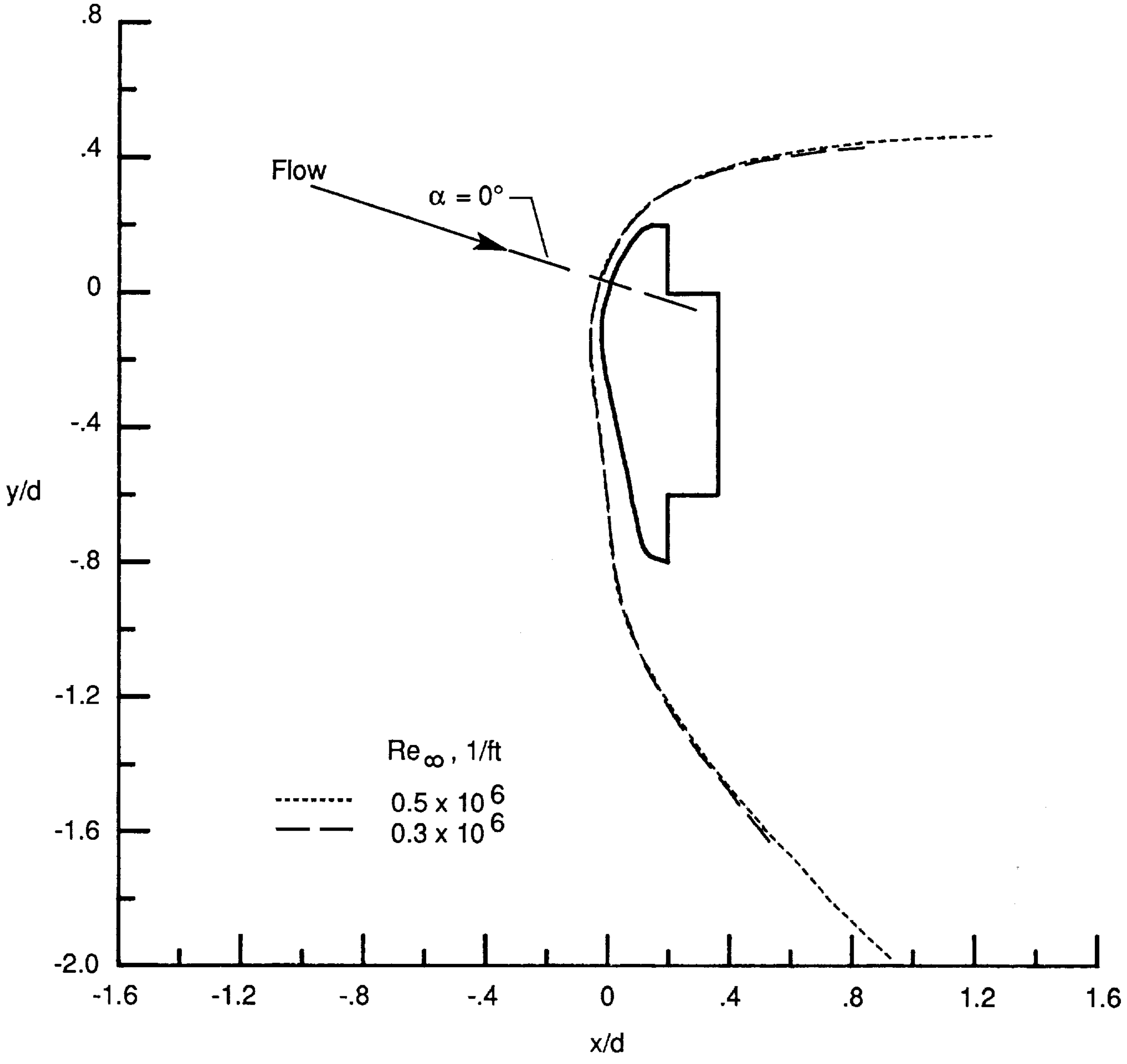

Figure 13. Effect of Re_∞ for $\alpha = 0°$ in Mach 6 CF_4.

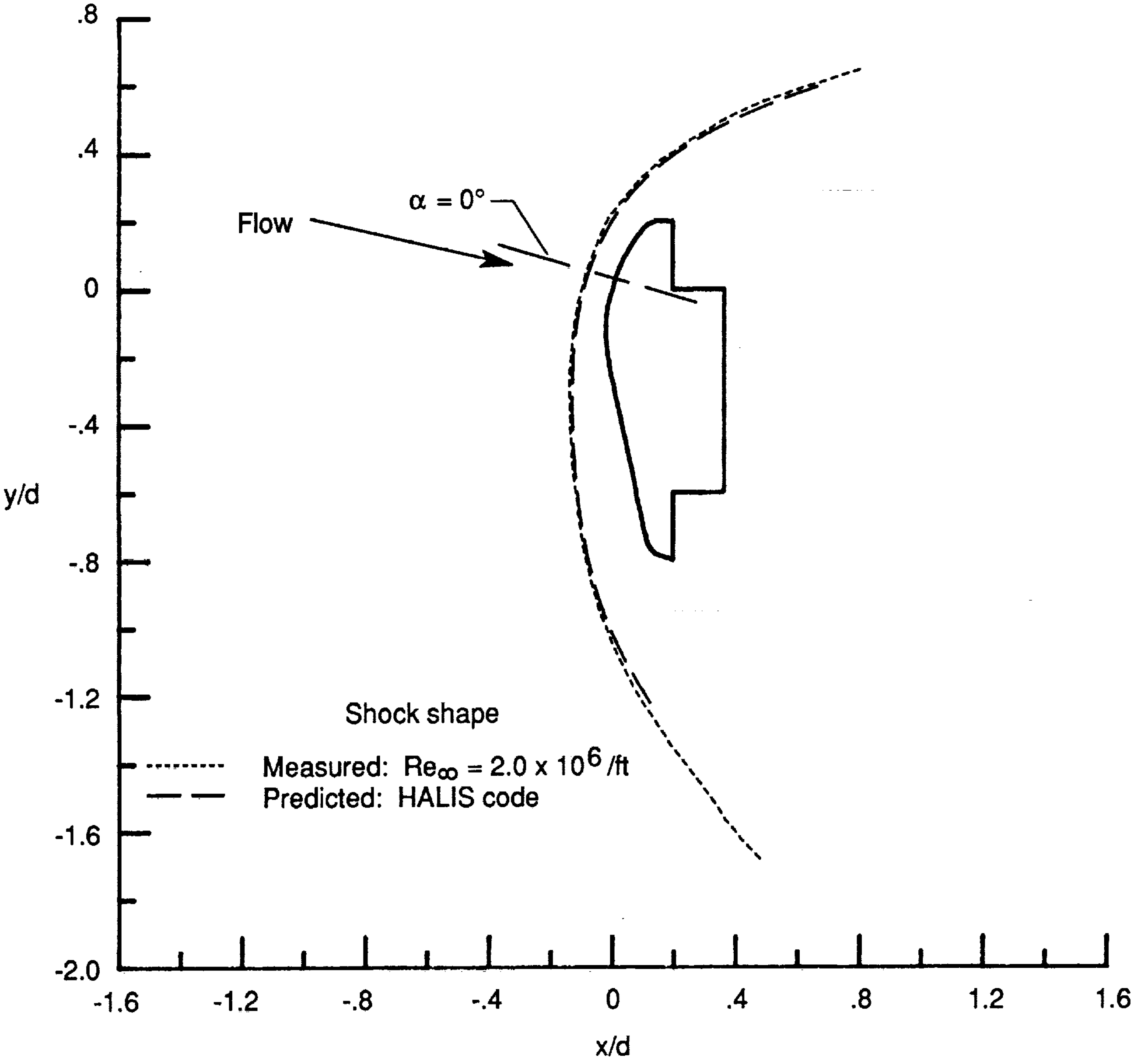

(a) $\alpha = 5°$.

Figure 14. Comparison of predicted and measured shock shapes in Mach 6 air.

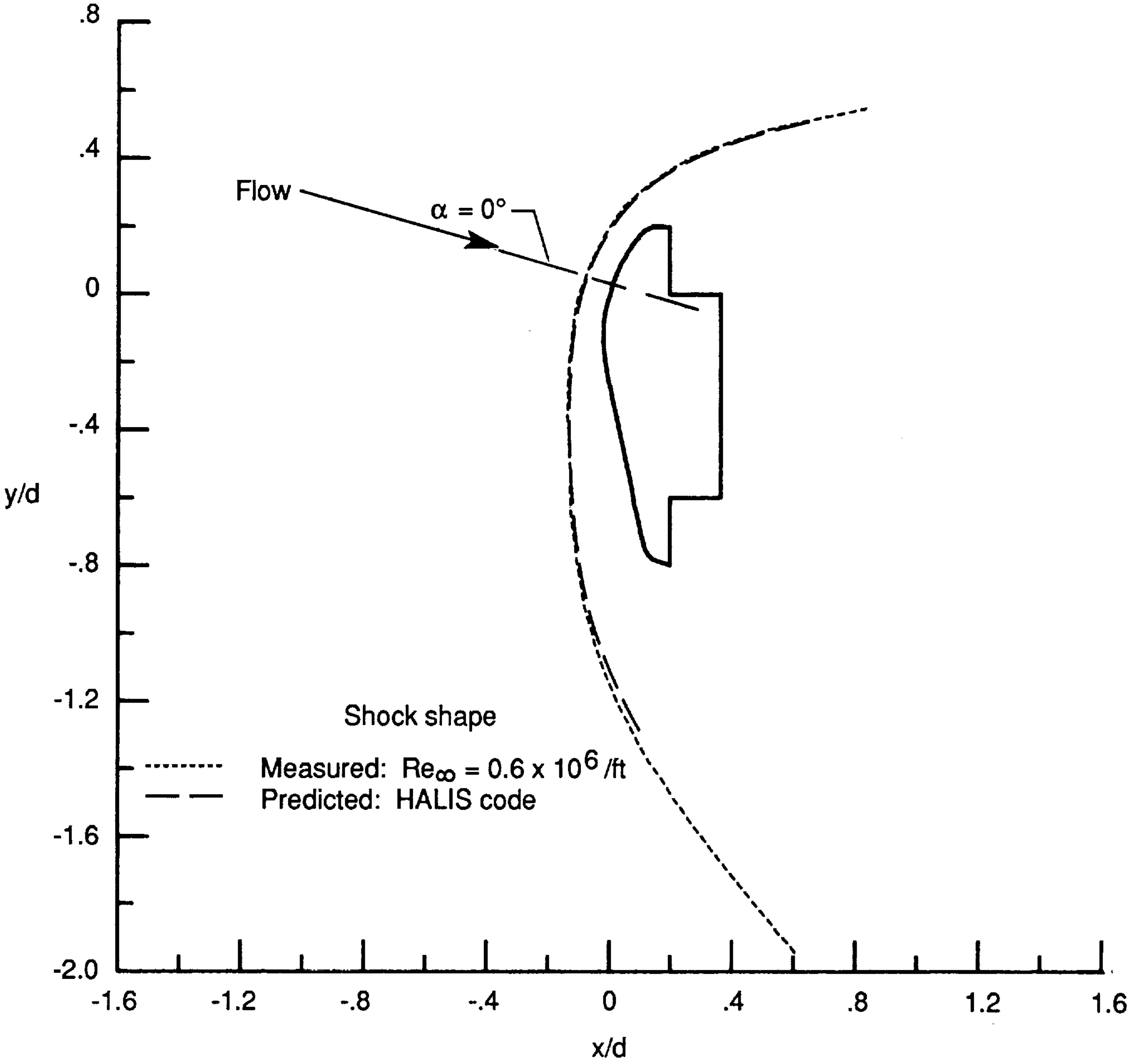

(b) $\alpha = 0°$.

Figure 14. Continued.

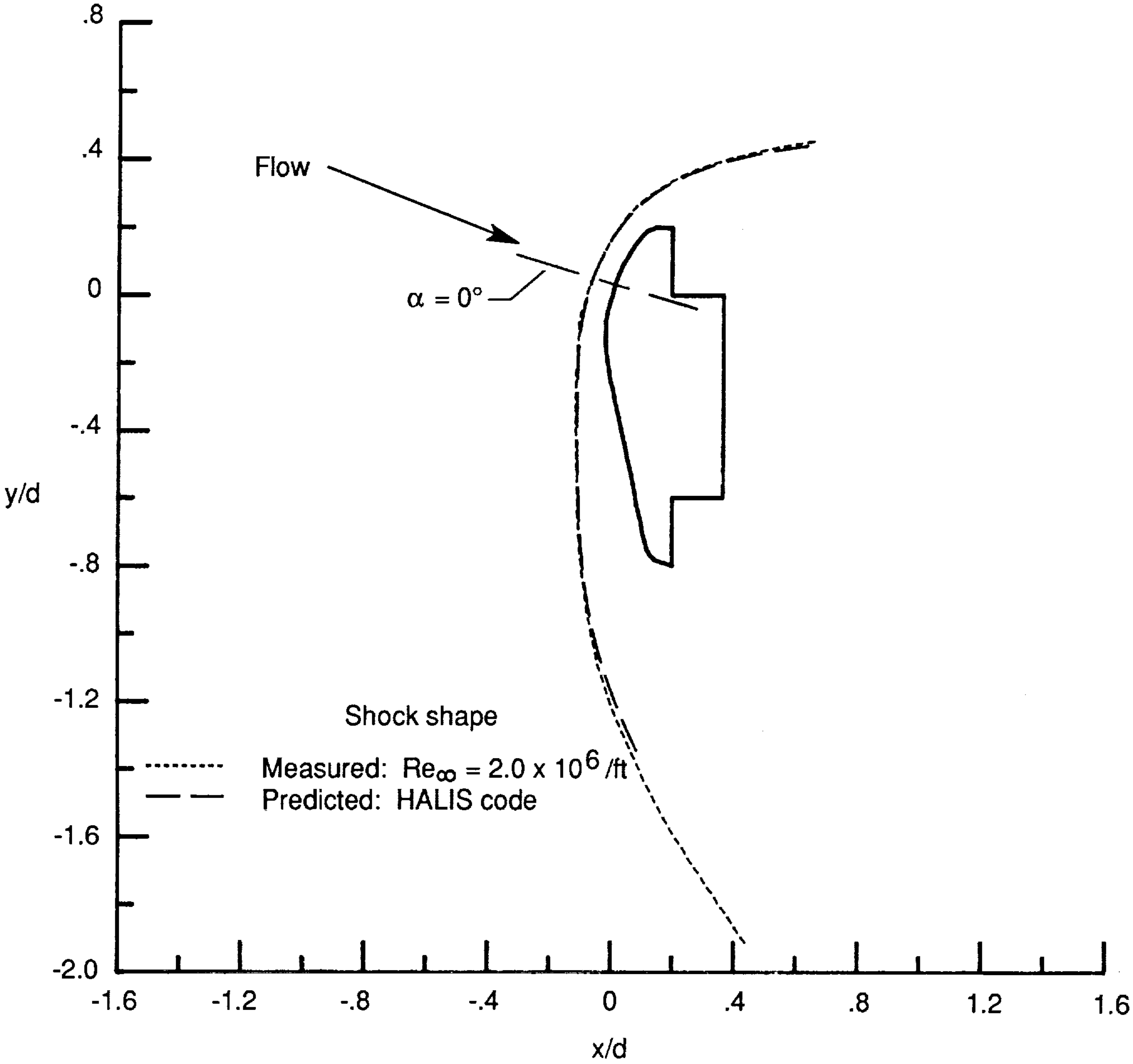

(c) $\alpha = -5°$.

Figure 14. Concluded.

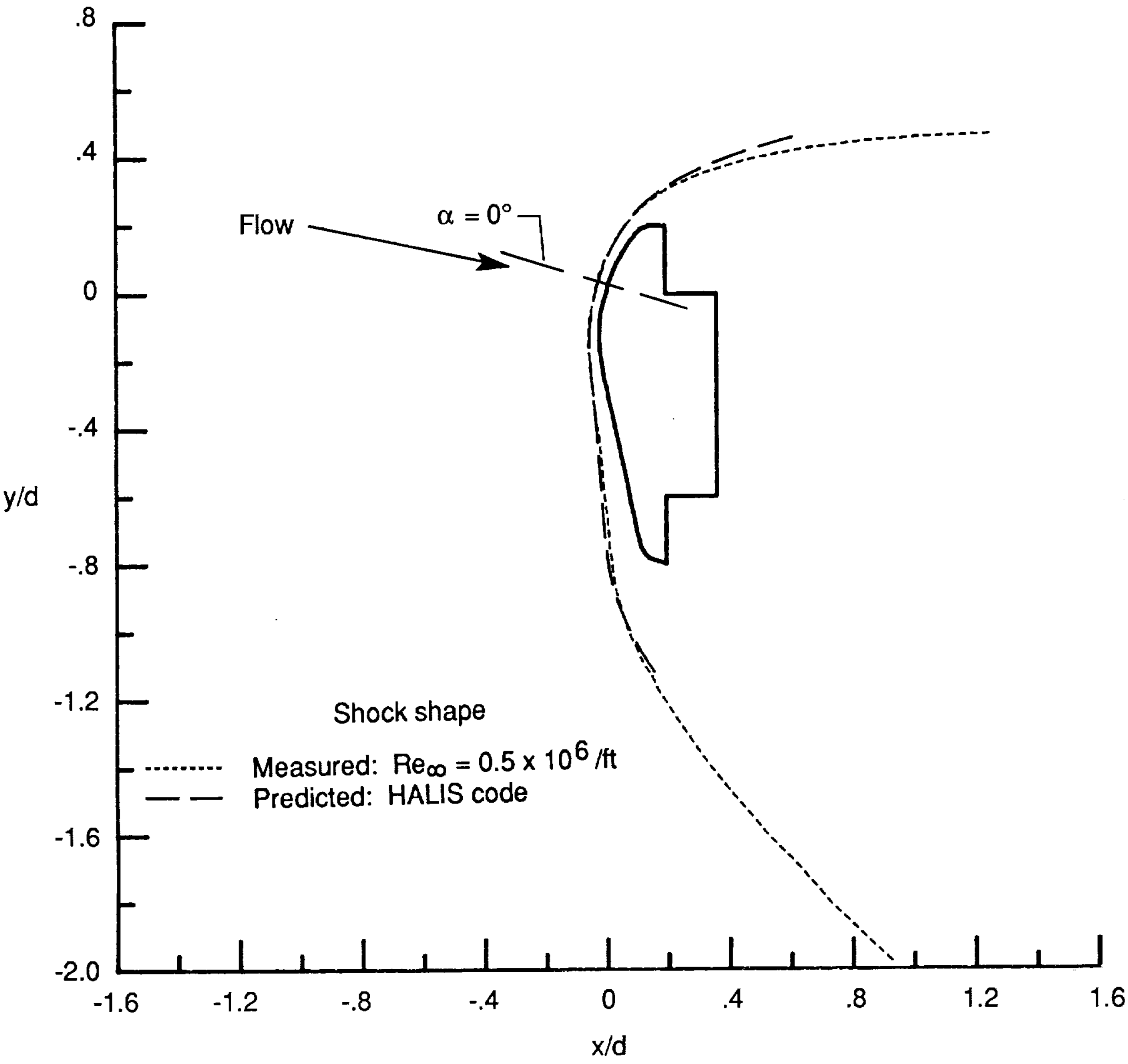

(a) $\alpha = 5°$.

Figure 15. Comparison of predicted and measured shock shapes in Mach 6.29 CF_4.

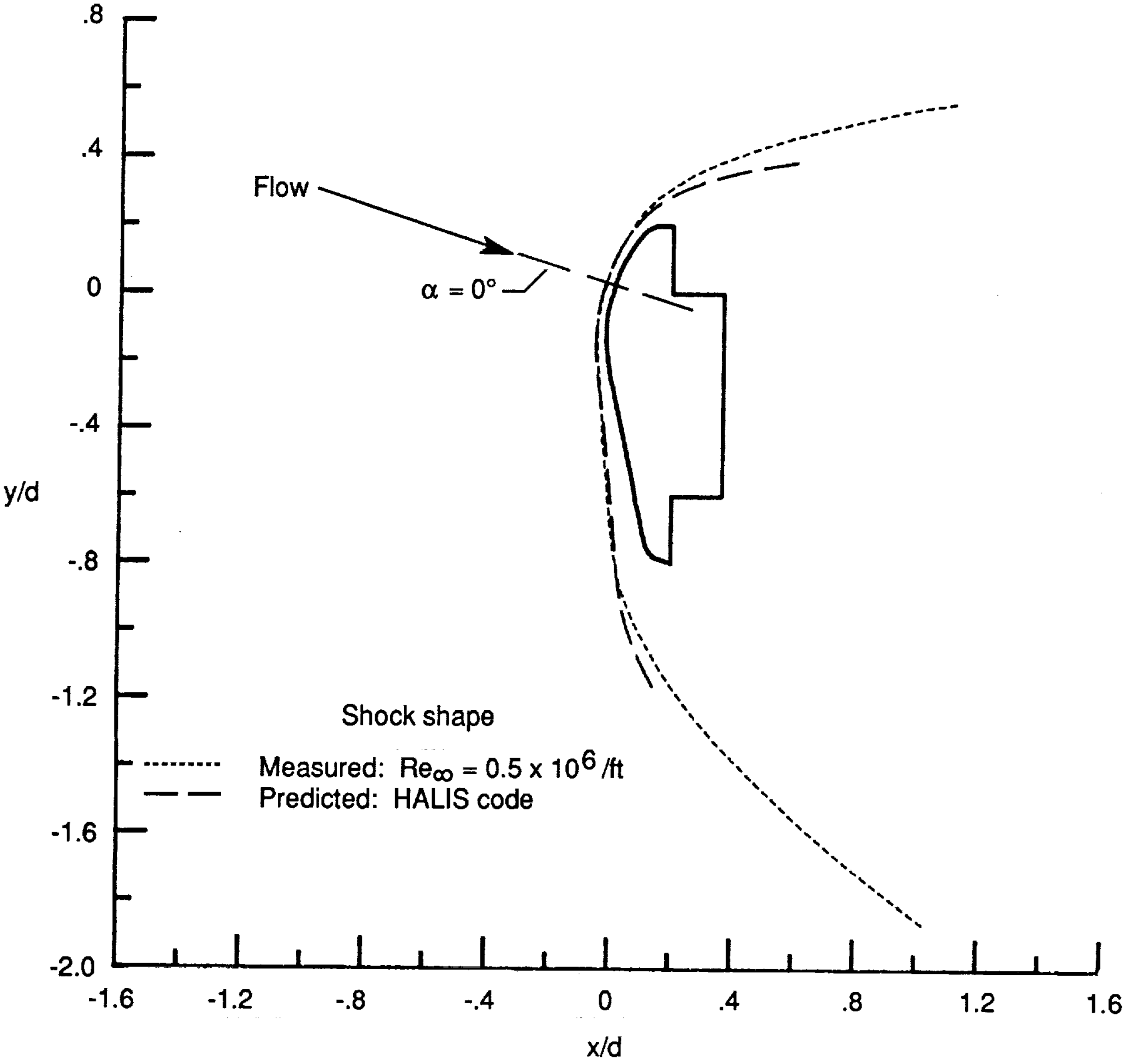

(b) $\alpha = 0°$.

Figure 15. Concluded.

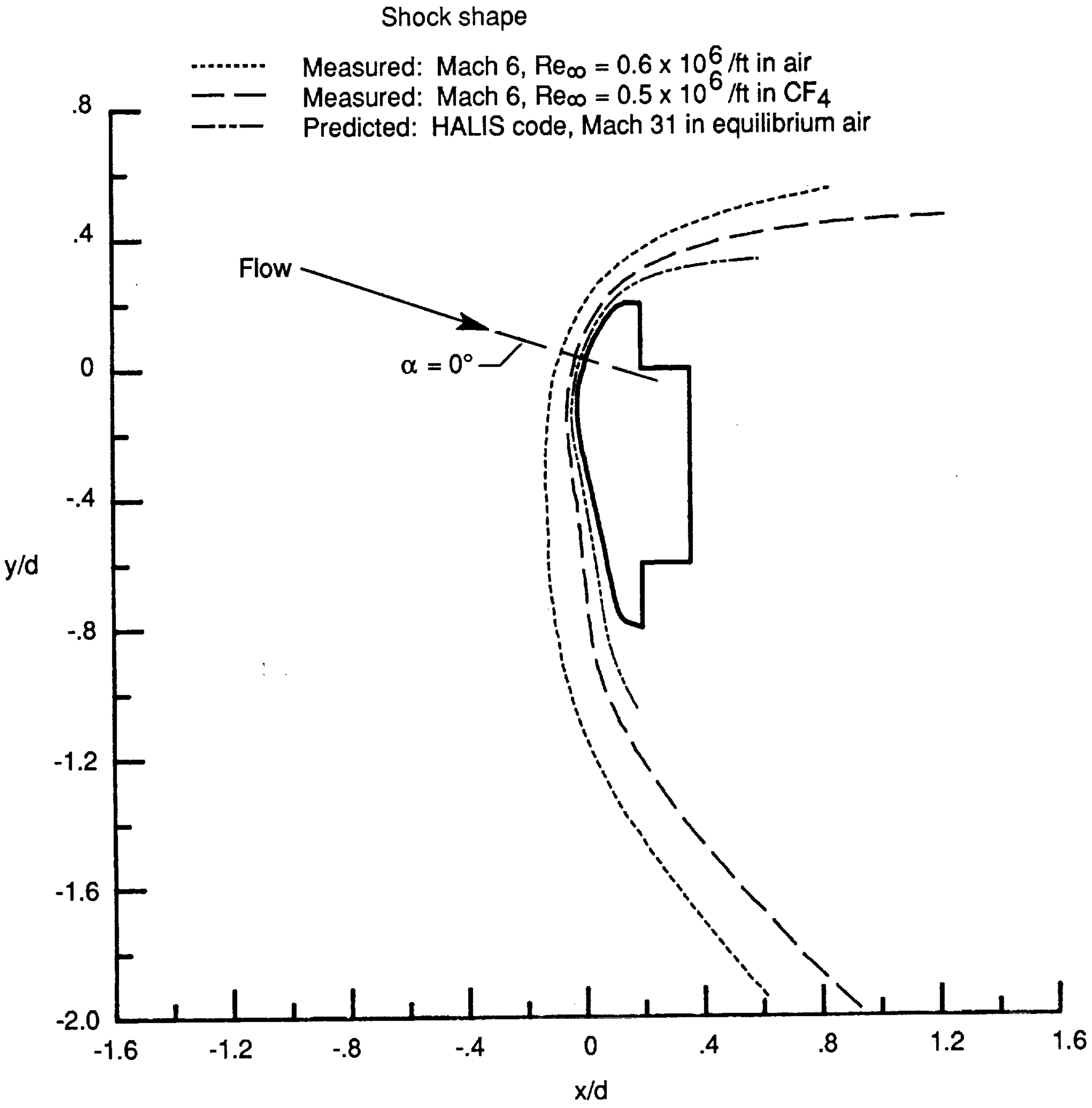

Figure 16. Comparison of predicted flight and wind-tunnel-measured shock shapes for $\alpha = 0°$.

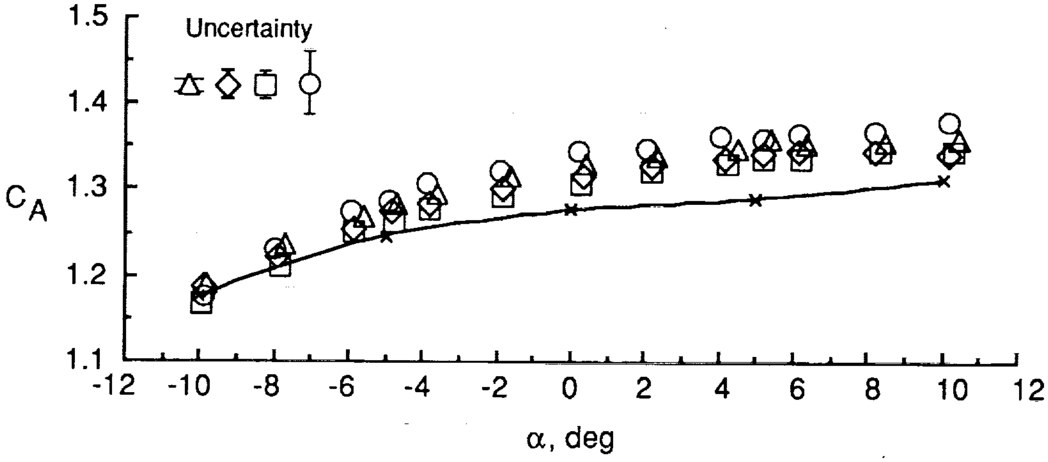

(a) Axial force coefficient.

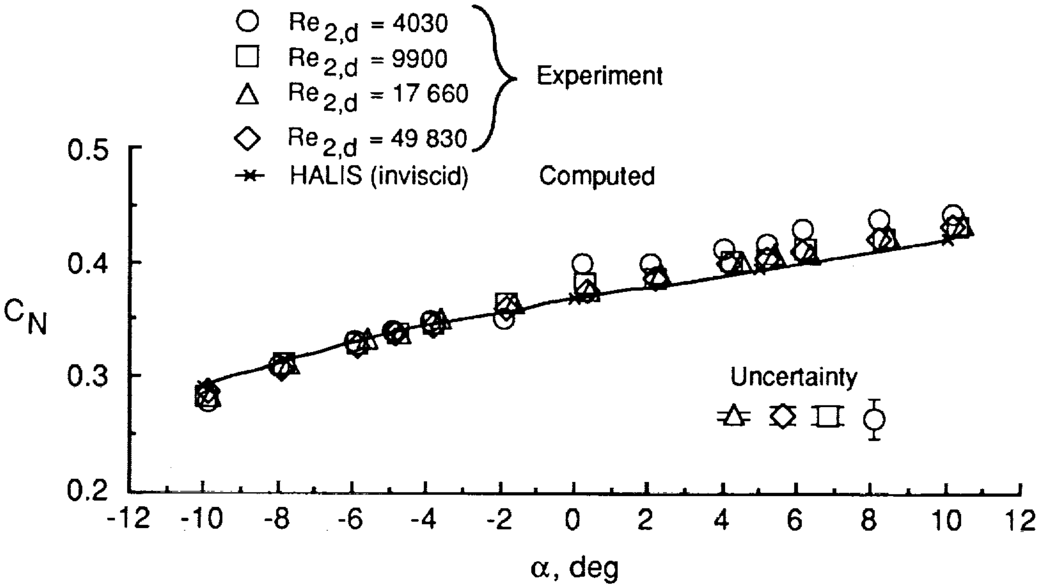

(b) Normal force coefficient.

Figure 17. Longitudinal aerodynamic coefficients in Mach 10 air with Reynolds number variation. $\beta = 0°$.

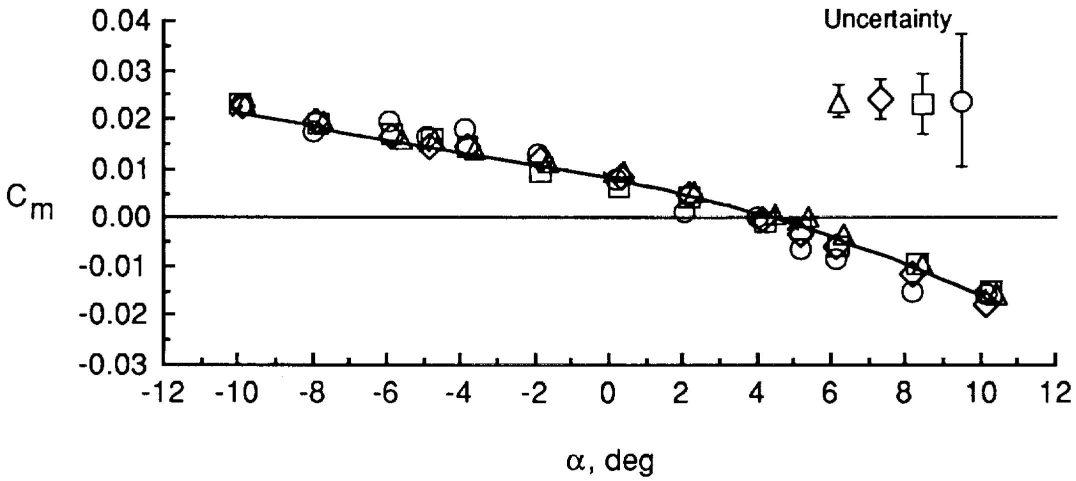

(c) Pitching moment coefficient.

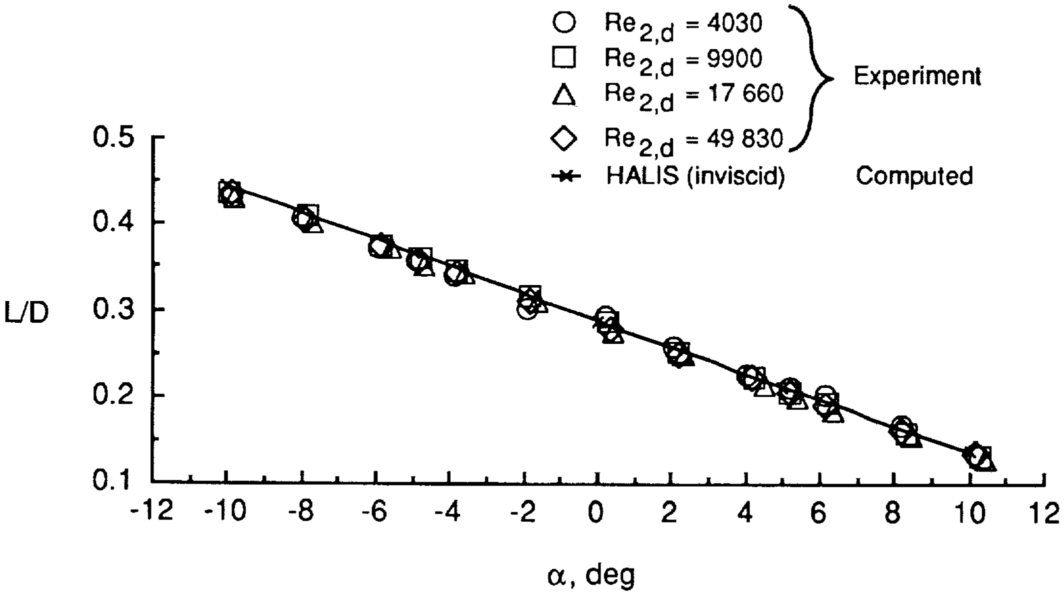

(d) Lift-to-drag ratio.

Figure 17. Concluded.

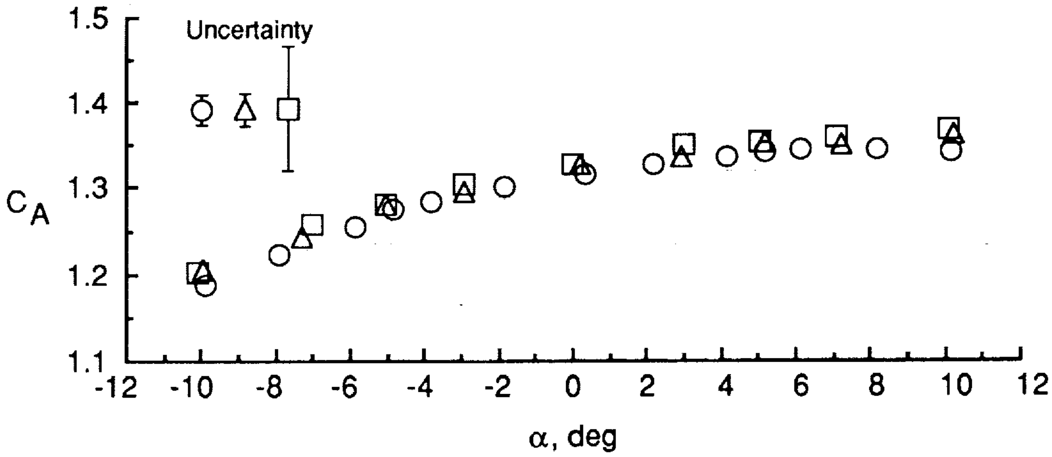

(a) Axial force coefficient.

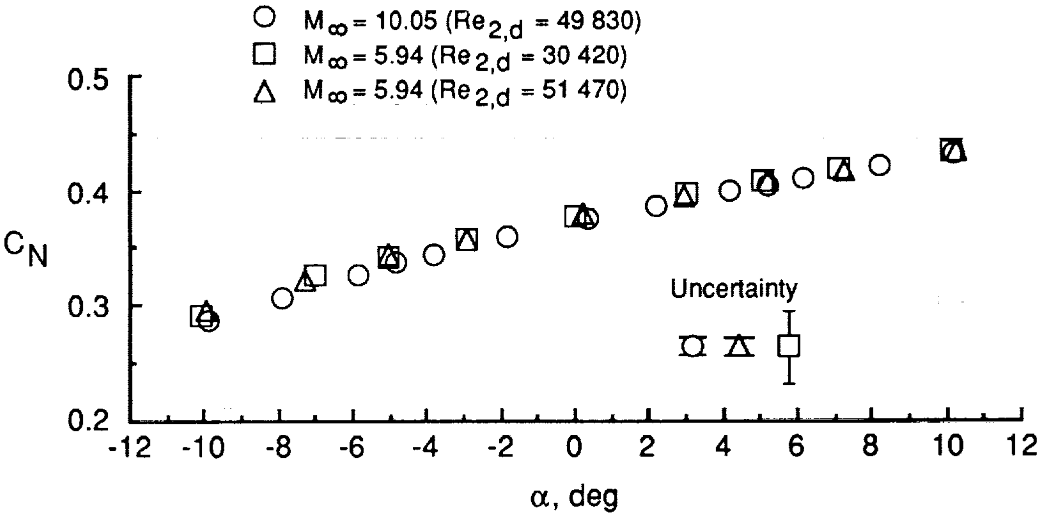

(b) Normal force coefficient.

Figure 18. Comparison of measured longitudinal aerodynamic coefficients for nominal Mach numbers of 6 and 10 in air. $\beta = 0°$.

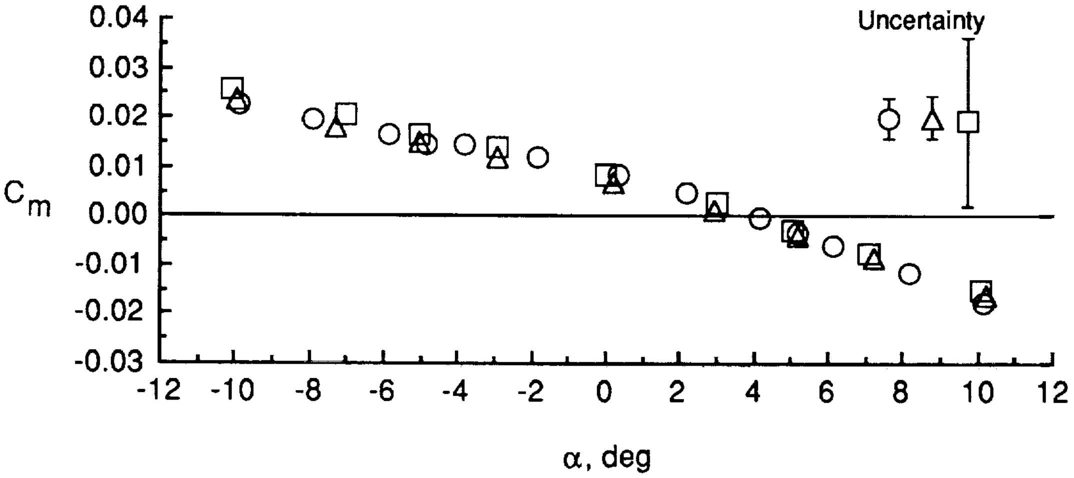

(c) Pitching moment coefficient.

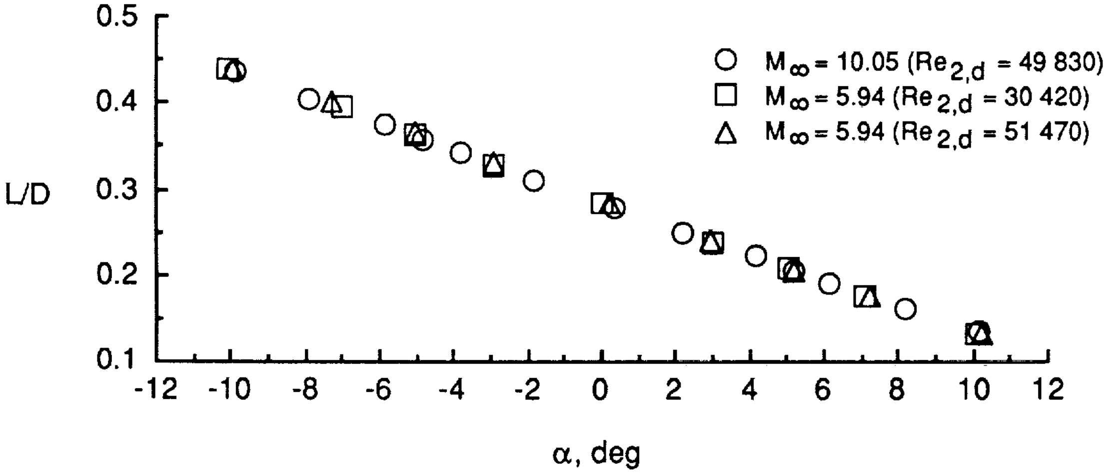

(d) Lift-to-drag ratio.

Figure 18. Concluded.

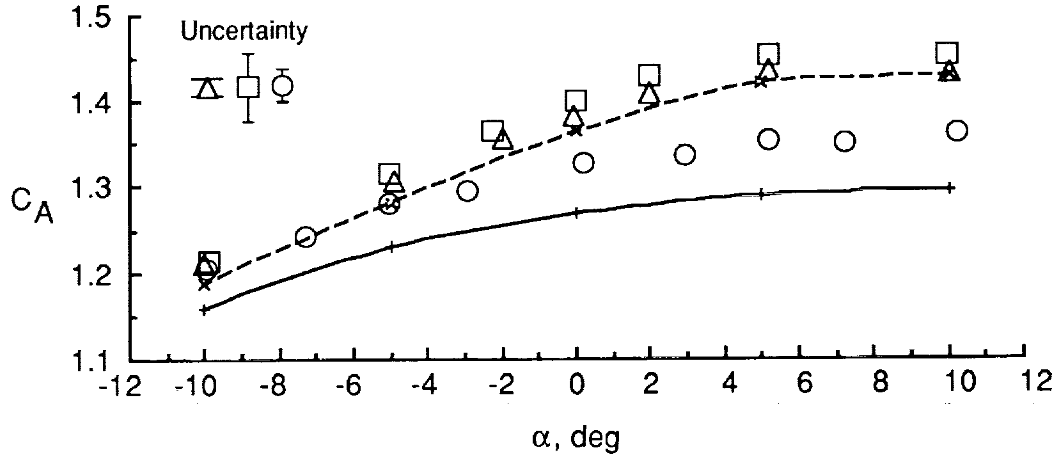

(a) Axial force coefficient.

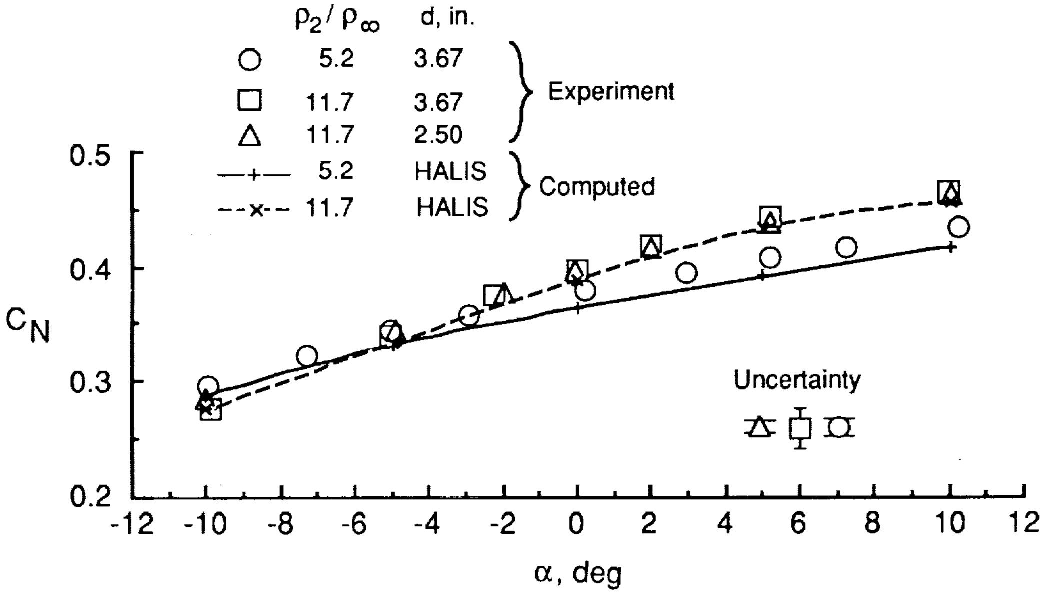

(b) Normal force coefficient.

Figure 19. Effect of density ratio across normal shock on longitudinal aerodynamic coefficients at Mach 6 and $\beta = 0°$.

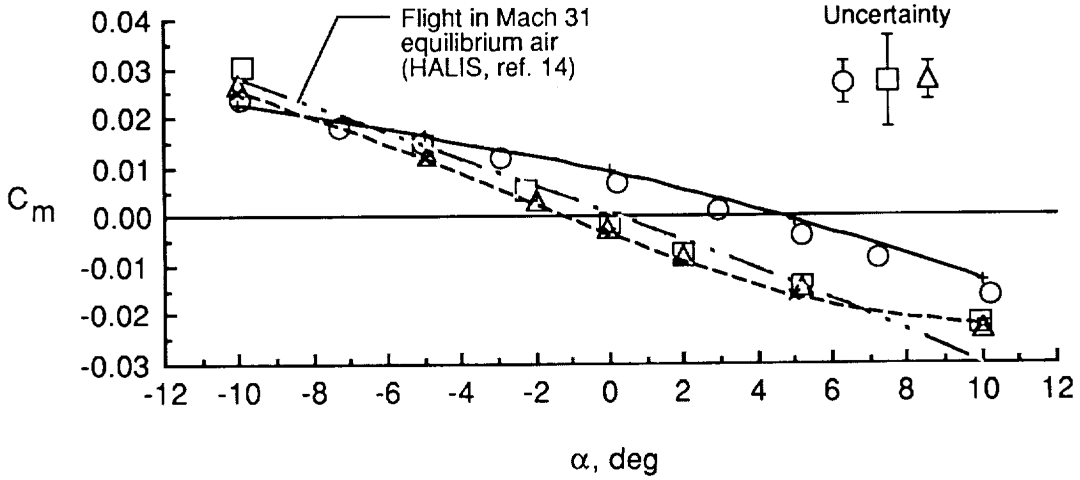

(c) Pitching moment coefficient.

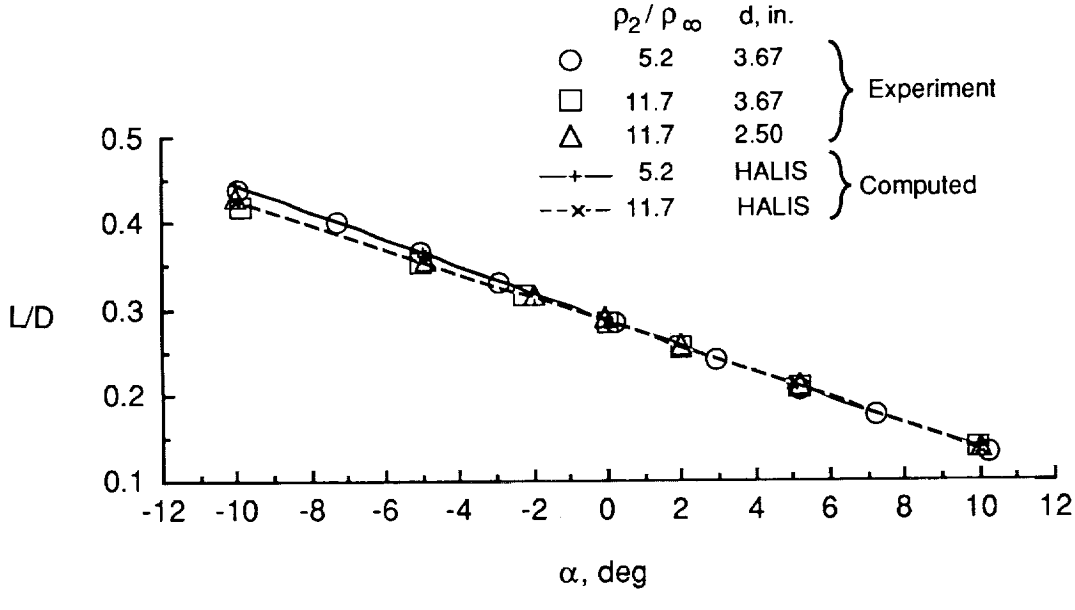

(d) Lift-to-drag ratio.

Figure 19. Concluded.

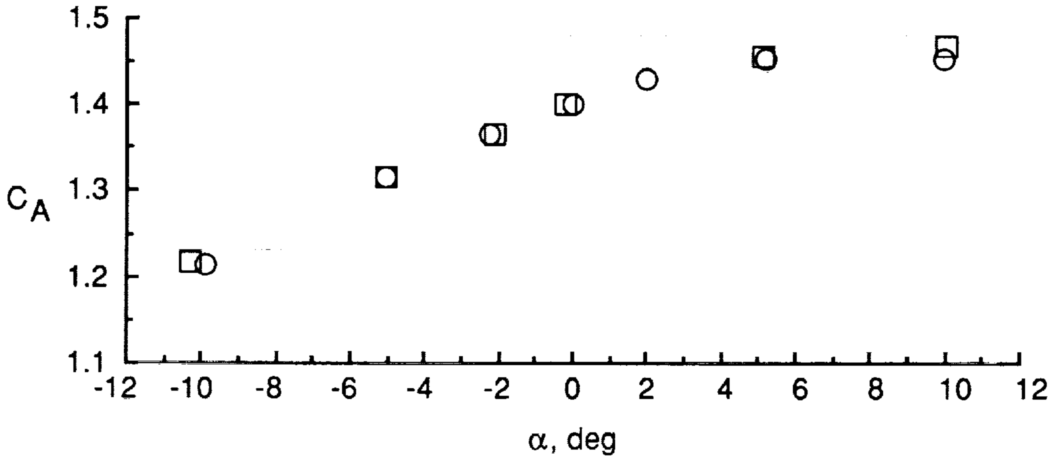

(a) Axial force coefficient.

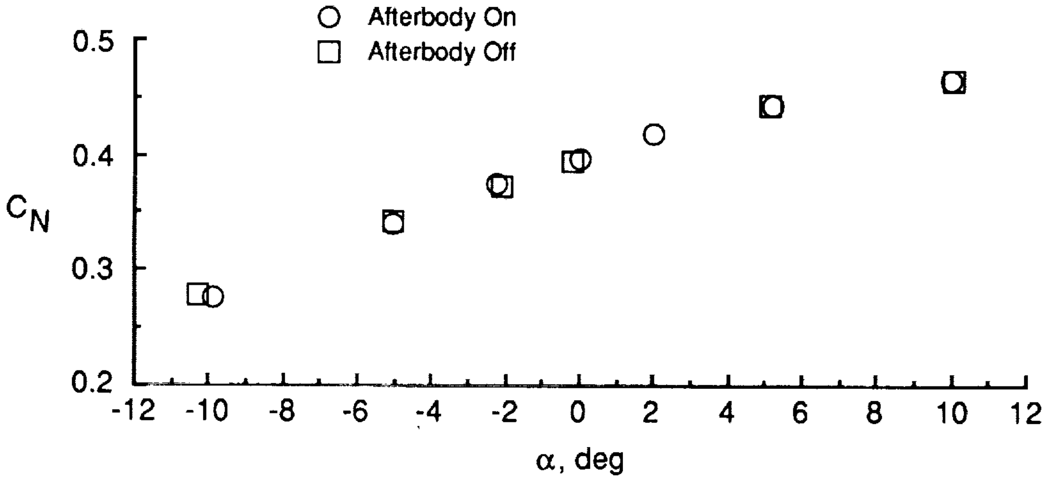

(b) Normal force coefficient.

Figure 20. Effect of presence of afterbody on longitudinal aerodynamic coefficients in Mach 6 CF_4. $\beta = 0°$.

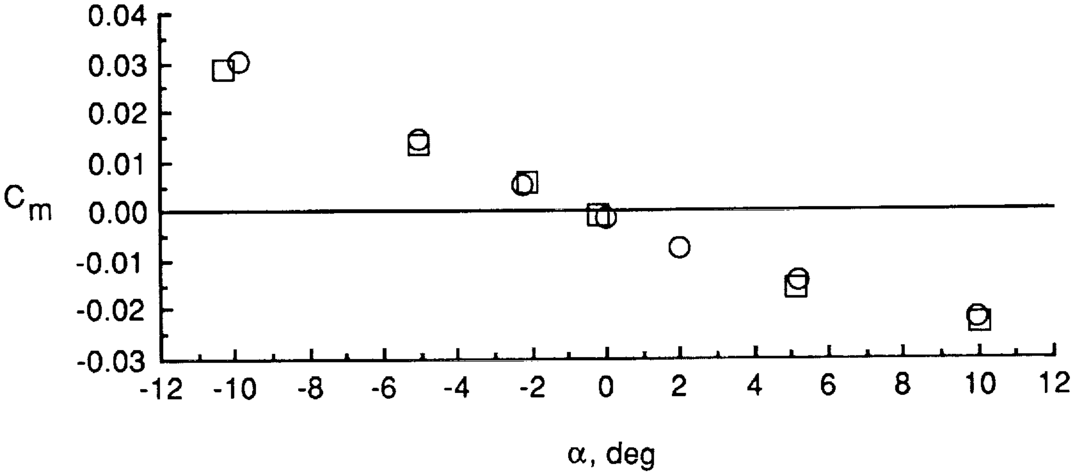

(c) Pitching moment coefficient.

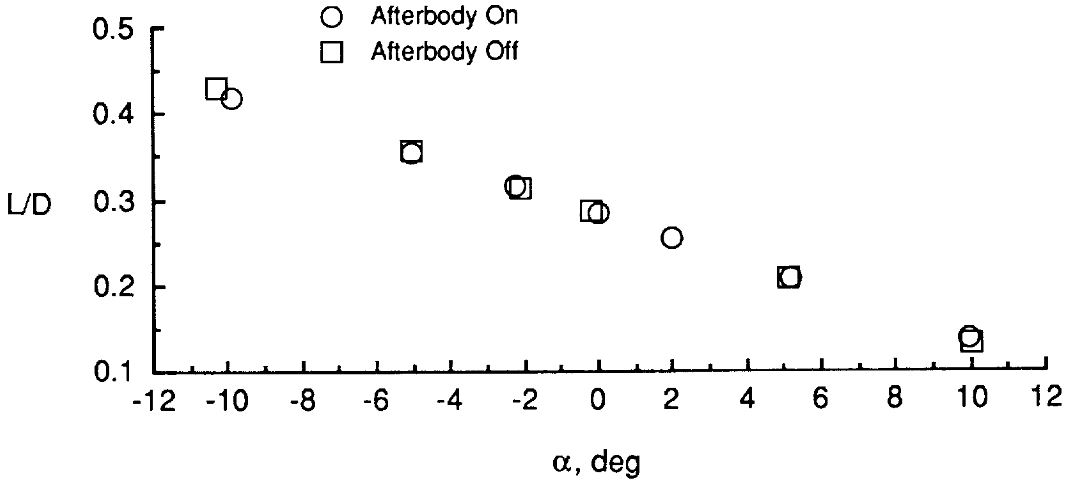

(d) Lift-to-drag ratio.

Figure 20. Concluded.

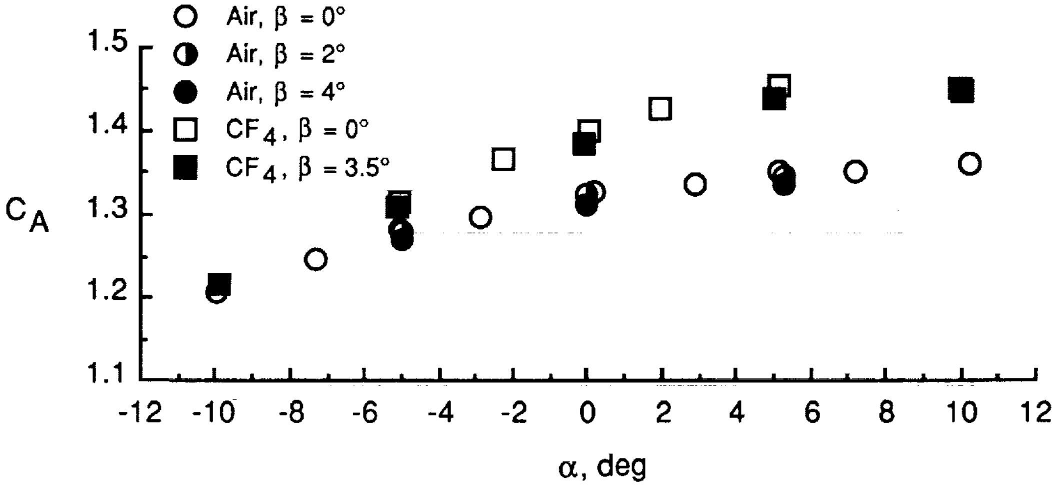

(a) Axial force coefficient.

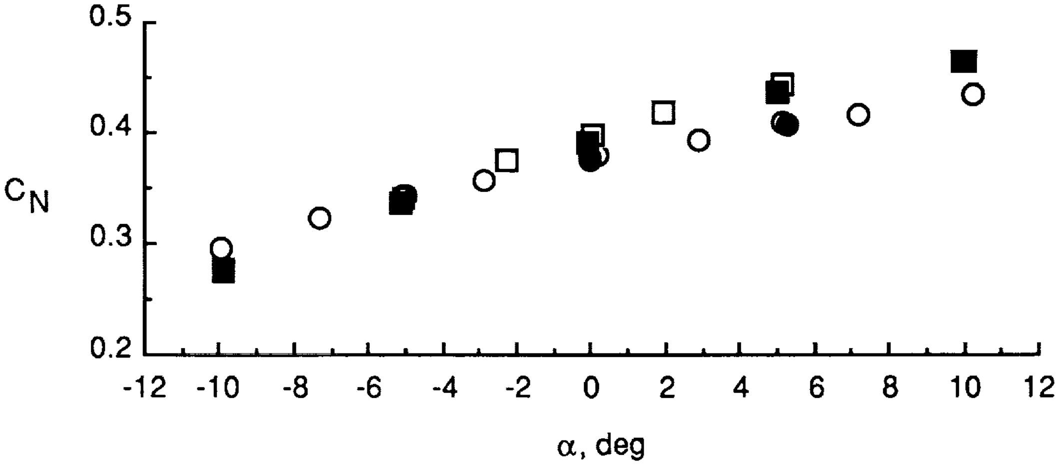

(b) Normal force coefficient.

Figure 21. Effect of sideslip angle β on aerodynamic coefficients and L/D in air and CF_4 at Mach 6.

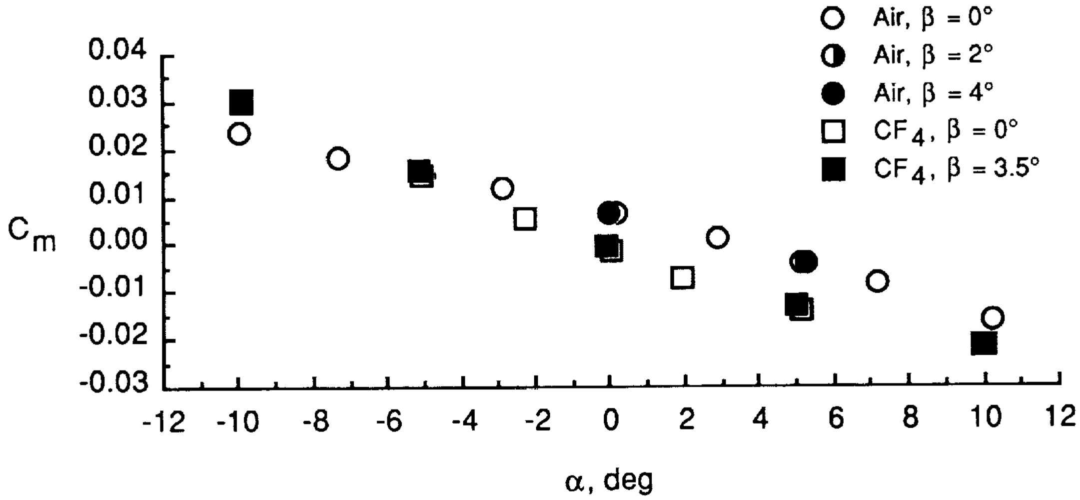

(c) Pitching moment coefficient.

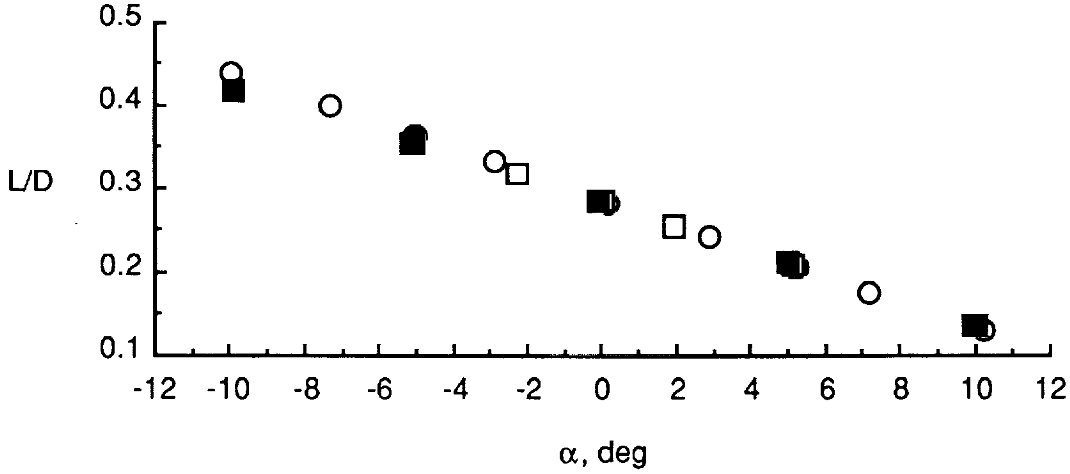

(d) Lift-to-drag ratio.

Figure 21. Concluded.

NASA
National Aeronautics and
Space Administration

Report Documentation Page

1. Report No.
NASA TP-2956

2. Government Accession No.

3. Recipient's Catalog No.

4. Title and Subtitle
Measured and Predicted Aerodynamic Coefficients and Shock Shapes for Aeroassist Flight Experiment (AFE) Configuration

5. Report Date
January 1990

6. Performing Organization Code

7. Author(s)
William L. Wells

8. Performing Organization Report No.
L-16644

9. Performing Organization Name and Address
NASA Langley Research Center
Hampton, VA 23665-5225

10. Work Unit No.
506-40-41-01

11. Contract or Grant No.

12. Sponsoring Agency Name and Address
National Aeronautics and Space Administration
Washington, DC 20546-0001

13. Type of Report and Period Covered
Technical Paper

14. Sponsoring Agency Code

15. Supplementary Notes

16. Abstract
Two scaled models of the Aeroassist Flight Experiment (AFE) vehicle were tested in two air wind tunnels and one CF_4 tunnel. The tests were to determine the static longitudinal aerodynamic characteristics and shock shapes for the configuration in hypersonic continuum flow. The tests were conducted over a range of angle of attack to evaluate the effects of Mach number, Reynolds numbers, and normal-shock density ratio.

17. Key Words (Suggested by Authors(s))
AFE
Hypersonic
Blunt body
Aerodynamic characteristics

18. Distribution Statement
Unclassified—Unlimited

Subject Category 02

19. Security Classif. (of this report)
Unclassified

20. Security Classif. (of this page)
Unclassified

21. No. of Pages
50

22. Price
A03

NASA FORM 1626 OCT 86

NASA-Langley, 1990

For sale by the National Technical Information Service, Springfield, Virginia 22161-2171